RESEARCH

Integrating of Nonlinear Shear Models into Fiber Element for Modeling Seismic Behavior of Reinforced Concrete Coupling Beams, Wall Piers, and Overall Coupled Wall Systems

Ke Du[1] , Huan Luo[1], Jiulin Bai[2*] and Jingjiang Sun[1]

Abstract

Reinforced concrete (RC) coupled wall systems, compared with RC shear wall without opening, have more complex nonlinear behavior under the extreme earthquake loads due to the existence of coupling beams. The behavior characteristics induced by nonlinear shear deformation such as shear–flexure interaction, pinching effect, strength and stiffness deterioration are clearly observed in numerous cyclic tests of RC coupling beams and shear walls. To develop an analytical model capable of accurately and efficiently assessing the expected seismic performance of RC coupled wall systems, it is critical to define the appropriate key components models (i.e., nonlinear models of RC wall piers/shear walls and coupling beams). Classic fiber beam element based on the theory of Euler–Bernoulli beam is frequently adopted to simulate the nonlinear responses of slender RC wall piers and coupling beams in the literature because it is able to accurately model the response characters from interaction of axial–bending moment at the section level. However, classic fiber beam element cannot capture the nonlinear behaviors of non-slender structures mainly controlled by nonlinear shear deformation. To overcome this shortcoming, a modified force-based fiber element (MFBFE) including shear effect is introduced and used as the analysis element of non-slender RC coupling beams and shear walls. At the section level, a novel shear model for RC coupling beams and an existed shear model for RC shear walls are respectively added to this fiber element to simulate nonlinear responses of these two key components. The analytical model for RC coupled walls hence is formed through integrating the proposed models of these two key components. The validations with different experimental results of cyclic tests including key components and structural system reported in the literature using these proposed models are performed. Good agreements are achieved for all of these proposed models via comparisons between predicted results and experimental data.

Keywords: reinforced concrete coupled wall systems, fiber element including shear effect, reversed-cyclic loading, nonlinear analysis, shear model

*Correspondence: baijiulin@cqu.edu.cn
[2] Key Laboratory of New Technology for Construction of Cities
in Mountain Area, Chongqing University, Ministry of Education,
Chongqing 400045, China
Full list of author information is available at the end of the article

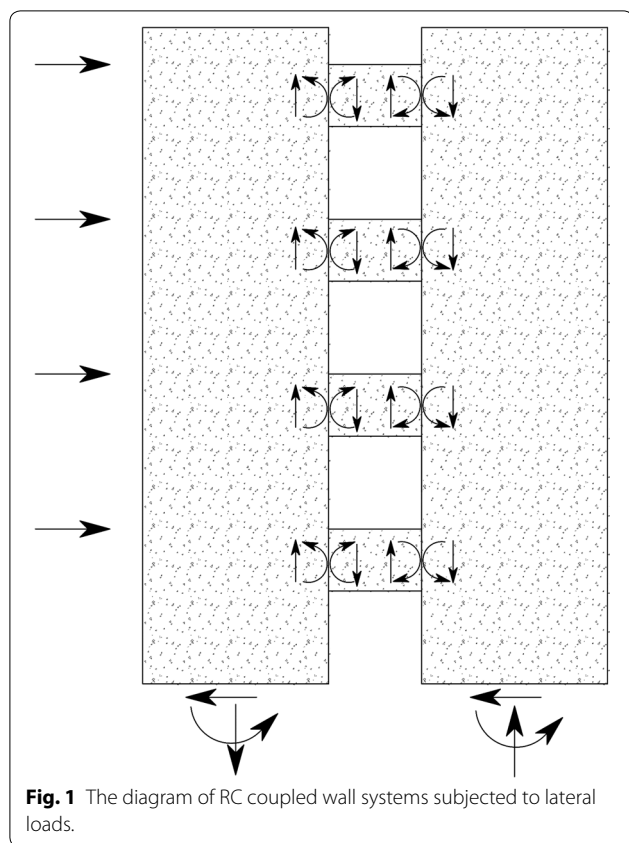Du *et al. Int J Concr Struct Mater*   (2019) 13:34

Page 2 of 26

1 Introduction

Reinforced concrete (RC) coupled wall systems consisting of RC wall piers and coupling beams are efficiently lateral forces resisting systems and can provide enough lateral stiffness for mid- to high-rise buildings to withstand earthquake-type loads. Recent earthquake investigations have demonstrated that this structural type is a reliable and robust design scheme to resist earthquake excitations. Compared to global collapse failure of RC frame structures subjected to strong ground motions, RC coupled walls are generally able to avoid complete collapse yet expose to local fractures in the key components such as shear failure of RC coupling beams and flexural failure at the bottom of wall piers. Shear brittle failure is sudden and unexpected, and occurs with no any symptoms, leading to serious risk for people's lives and property. As such, engineers and researchers all dedicate to developing effective and reliable strategies to forbid occurrence of such danger failure modes. ACI building code (ACI-318-11 2011) indicates that RC coupling beams with aspect ratio less than 2 and shear stress demand greater than $0.33 \sqrt{f_c'}$ MPa ($4 \sqrt{f_c'}$ psi) need to be arranged a special diagonal reinforcement layout to prevent the occurrence of shear failure, where f_c' is the compressive strength of concrete.

Wall piers behavior is generally classified according to wall aspect ratio (AR), as either shear-controlled (AR less than 1.0–1.5) or flexure-controlled (AR greater than 2.5–3.0). For walls between these aspect ratios (referred to as moderate aspect ratio walls), nonlinear responses associated with both axial/bending and shear behavior. Recently, a large number of experimental investigations have shown that flexural and shear yielding of moderate aspect ratio walls occur near-simultaneously, even this interaction has been observed on slender RC walls with aspect ratios greater than 2.0 (Wang et al. 1975; Vallenas et al. 1979; Hines et al. 1995, 2002; Sayre 2003; Thomsen and Wallace 2004; Massone et al. 2004; Dazio et al. 2009; Lowes et al. 2012). This interaction between nonlinear flexural and shear behavior, commonly referred to as shear–flexure interaction. Coupling beam behavior is commonly judged according to span–depth ratio. The results obtained from the test conducted by Paulay (1971) on conventionally reinforced coupling beams presented dominant shear behavior with span–depth ratios of 1.02 and 1.29. Failure mechanisms such as diagonal tension or sliding shear were encountered during the tests. Jun et al. (2018) pointed that coupling beams with a span–depth ratio of no more than 2.5 tend to fail in shear-dominant rather than in flexure. Fisher et al. (2018) presents the results from a recent experiment on a coupling beam at the University of Toronto. The results show that a flexure-only analysis would account for only 53% of the total

predicted deformation. Addition of the effect of curvature resulting from shear (but not shear strain) increases the predicted percentage to 57%, while, inclusion of shear strains increases the percentage to 100%. To improve the ductility of concrete coupling beams and to suppress the shear failure mode, many studies have been carried out through last decades (Paulay 1974; Tassios et al. 1996; Galano and Vignoli 2000; Lequesne et al. 2012; Han et al. 2015). These experimental studies revealed that coupling beams, when they are diagonally reinforced with enough confinement, can provide adequate stability and excellent ductility.

Numerical analysis has been developed to simulate the seismic behavior of coupled wall systems by many researchers (Takayanagi and Schnobrich 1979; Saatcioglu et al. 1983; Hung and El-Tawil 2011; Hung 2012; Eljadei and Harries 2014; Fox et al. 2014; Harries et al. 2004; Vuran and Aydinoglu 2016; Kim 2016; Kim and Choi 2017). In the reference (Takayanagi and Schnobrich 1979), researchers developed a model used for nonlinear static and dynamic analyses of a 10-story coupled wall structure, in which wall piers and coupling beams were simulated with line elements, and the two ends of every line element defined zero-length springs with assigning the corresponding inelastic materials that was used for modeling the plastic hinges. Saatcioglu et al. (1983) performed nonlinear dynamic analysis of a 20-story coupled wall structure with the scheme that each structural member was idealized as a line element and inelastic behavior was simulated through defining plasticity hinges at member ends; each hinge was designated a hysteretic model that incorporates effects of axial force-moment interaction, shear yielding, strength degradation, pinching, reloading and unloading branches of hysteresis loops. Hung (2012) implemented the hybrid simulation strategy of a 12-story composite coupled wall system in which the displacement-based beam column element was employed to simulate RC shear walls and steel coupling beams respectively; the shear wall cross section was modeled using fiber sections and the steel coupling beams were modeled with considering nonlinear shear and flexural behaviors through the tactic that the moment of inertia of the full cross section was used for bending and the full web area was used for shear; however, the shear behavior of wall was not taken into account in this scheme. Eljadei and Harries (2014) conducted nonlinear static (pushover) and dynamic analyses of a 12-story prototype coupled wall structure; the wall piers were modeled using a general quadratic beam-column model, and the Giberson one-component beams were used for representing the coupling beams. Fox et al. (2014) proposed a simplified capacity design method, with which nonlinear time-history analyses of a set of 15 coupled walls were performed;

Du *et al. Int J Concr Struct Mater* (2019) 13:34

Page 3 of 26

Fig. 1 The diagram of RC coupled wall systems subjected to lateral loads.

the flexural and axial responses of coupled walls were simulated by distributed plasticity fiber beam elements with defining the nonlinearity materials at the section level, and additional transverse springs between wall elements were chosen to model shear response of coupling beams; nevertheless, these transverse springs just exhibit linear shear behaviors.

Although aforementioned models can represent the inelastic dynamic characteristics of RC coupled walls, there are many shortcomings that need to be resolved. Especially considering the shear–flexure interaction and nonlinear shear deformation in nonlinear models used for predicting the static cyclic behaviors of RC coupling beams, wall piers, and overall coupled wall systems are not presented in the mentioned models. To develop an analytical model that is able to accurately represent the static cyclic behavior of RC coupled wall systems, the models of RC coupling beams and wall piers must be selected reasonably. This is because the resistant mechanism of coupled wall systems is exhibited through a combination of flexural behavior of wall piers and frame action contributed by coupling beams (axial forces from wall piers are transferred to coupling beams and lead to a frame character, as shown in Fig. 1), and the behavior performances of coupling beams and wall piers have

a great influence on the overall response of a coupled wall system (Harries et al. 2004). As the shear stresses occurred in the non-slender RC coupling beams and wall piers are generally large, the shear response of these two key components in a coupled wall system needs to be taken into account when building their finite element (FE) models.

By reviewing the existed coupled wall models above (Takayanagi and Schnobrich 1979; Saatcioglu et al. 1983; Hung and El-Tawil 2011; Hung 2012; Eljadei and Harries 2014; Fox et al. 2014; Harries et al. 2004; Vuran and Aydinoglu 2016), they can be classified as two categories, that is, lumped plasticity models and distributed nonlinearity models. It has been validated that the distributed plasticity models (e.g., classic fiber beam elements) can not only reflect the real plasticity development but produce the accurate response results of RC structures under both static and dynamic loads (Spacone et al. 1996). Classic fiber beam elements (i.e., displacement-based and force-based fiber elements) based on the cross-sectional discretization in a series of fibers have been developed to simulate nonlinear responses of RC structures governed by flexural deformation. With assigning the corresponding uniaxial constitutive models at the section level, the section behavior under axial and bending forces is captured through integrating fiber stresses over the whole cross-section. However, classic fiber beam elements are not capable of considering shear stresses, and thus shear behavior at the section level cannot be directly acquired. To eliminate this limitation, many researchers carried out various studies by introducing the Timoshenko beam theory into the force-based fiber element (FBFE) due to its simplicity, efficiency, and robustness to account for the shear effects of RC structures (Petrangeli et al. 1999; Marini and Spacone 2006). Petrangeli et al. (1999) successfully conducted a fiber section model that can allow for shear stresses, deformations, and stiffness at the section level using a new concrete law based on micro-plane theory. But this model demands extra computation cost at the section level because the additional equilibrium is imposed. A two-dimensional (2D) modified force-based fiber beam element (MFBFE) allowing for uniaxial bending and shear effect based on the Timoshenko beam theory is introduced by (Marini and Spacone 2006), in which the axial and bending responses follow the traditional fiber section model, and shear effect is simulated by a nonlinear V-γ constitutive law at the section level. The shear deformation is decoupled from axial and bending effects in the section stiffness. The shear and flexural forces, nonetheless, are coupled at the element level because of enforced equilibrium along the element. It is noteworthy that this strategy has an unrivaled advantage in simulating shear-critical components, because

Du *et al. Int J Concr Struct Mater*   (2019) 13:34

Page 4 of 26

the element bending moments are constrained by the element shear forces if shear failure at the section level occurs before flexural failure. A large number of numerical analyses of RC structures have been conducted considering flexure-shear interaction using modified force-based fiber beam element (Ferreira et al. 2014; Correia et al. 2015; Almeida et al. 2015; Lucchini et al. 2017; Zimos et al. 2018; Feng and Xu 2018; Bitar et al. 2018). However, these models were developed for RC beams and columns, not suit for coupled walls.

To develop simple, accurate, and efficient models capable of capturing the cyclic behaviors of key components (i.e., diagonally reinforced coupling beams and RC wall piers) and overall coupled wall systems, new modified force-based beam element (MFBBE) and wall element (MFBWE) composed of MFBFE and shear models were developed in MATLAB (2014). This paper presents the formulations of MFBBE and MFBWE, and also the nonlinear force–deformation constitutive laws of concrete, reinforcement bars, and shear models used in these formulations. To examine the efficiency, stability, and accuracy of MFBBE and MFBWE, comparisons with the existed test data of the key components (Lequesne et al. 2012; Han et al. 2015; Gulec and Whittaker 2009) are performed. As confinement effect of the stirrups can improve the plasticity deformation capacity of RC structures, appropriate confined concrete models (Mander et al. 1988; Legeron and Paultre 2003) for the nonlinear cyclic simulation are thus discussed and summarized. At last, a comprehensive structural system model named CWE for RC coupled wall, integrating MFBBE and MFBWE, is proposed and validated through comparison with the experimental data of cyclic tests of two RC coupled wall specimens.

2 Formulation of the MFBFE

The MFBFE including a nonlinear section model for shear behavior presented herein is based on the FBFE originally developed by [15]. The total nodal forces $\mathbf{Q}$ at two end nodes of the MFBFE shown in Fig. 2, and section forces $\mathbf{D}(x)$ and deformations $\mathbf{d}(x)$ at the x location along the length L of the MFBFE are grouped in the following arrays, respectively. The torsion deformation in this element is assumed to remain linear elastic.

$$\mathbf{Q} = \begin{bmatrix} M_{1y} & M_{1z} & M_{2y} & M_{2z} & N & T \end{bmatrix}^{\mathrm{T}}$$

$$\mathbf{D}(x) = \begin{bmatrix} M_y(x) & M_z(x) & V_y(x) & V_z(x) & N(x) & T(x) \end{bmatrix}^{\mathbf{T}}$$

$$\mathbf{d}(x) = \begin{bmatrix} \chi_y(x) & \chi_z(x) & \gamma_{xy}(x) & \gamma_{xz}(x) & \varepsilon(x) & \gamma_t(x) \end{bmatrix}^{\mathbf{T}}$$
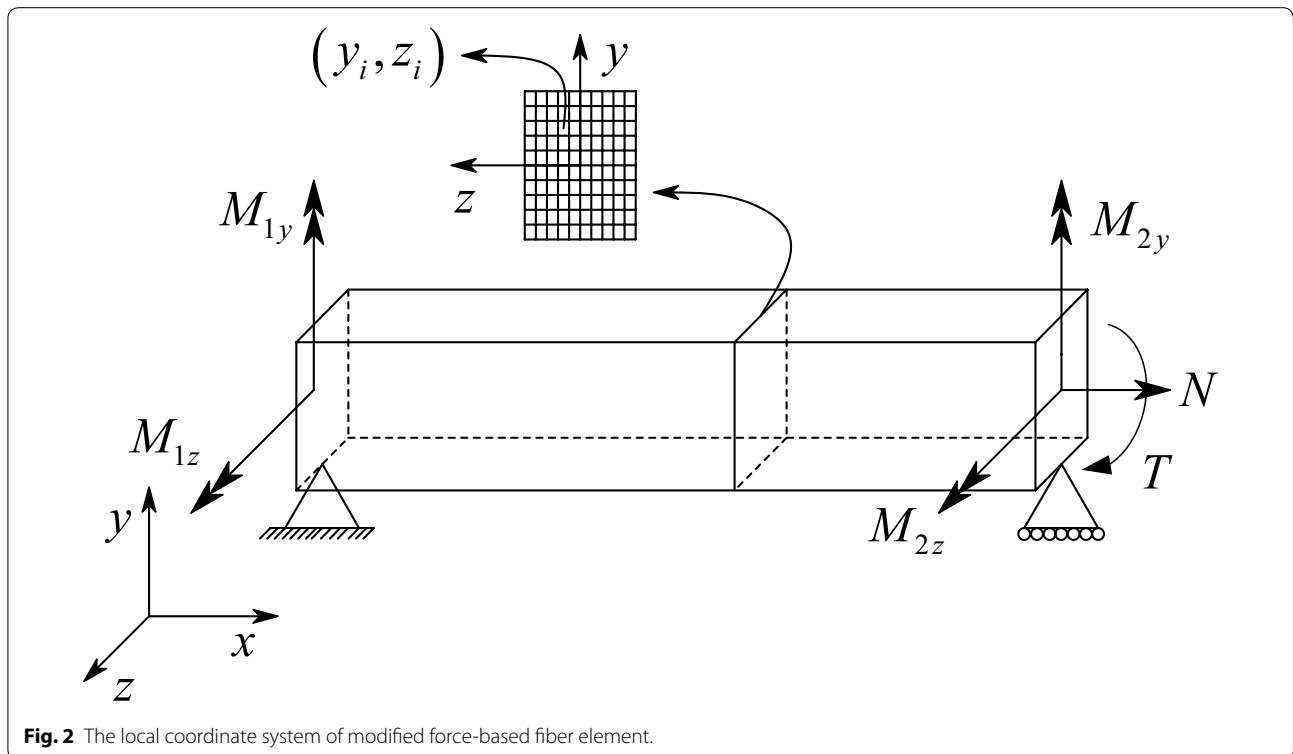

Fig. 2 The local coordinate system of modified force-based fiber element.

The equilibrium equation at the element level relates the nodal forces $\mathbf{Q}$ with the section forces $\mathbf{D}(x)$, that is, the bending moments $M_y(x)$ and $M_z(x)$ about the y and z axes, the shear forces $V_y(x)$ and $V_z(x)$ along the y and z axes, the axial force N, and the torsional moment T, respectively. The equilibrium equation is given by

$$\mathbf{D}(x) = \mathbf{b}(x)\mathbf{Q} \tag{1}$$

where $\mathbf{b}(x)$ is the force interpolation functions defined as

$$\mathbf{b}(x) = \begin{bmatrix} \frac{x}{L}-1 & 0 & \frac{x}{L} & 0 & 0 & 0 \\ 0 & \frac{x}{L}-1 & 0 & \frac{x}{L} & 0 & 0 \\ \frac{1}{L} & 0 & \frac{1}{L} & 0 & 0 & 0 \\ 0 & \frac{1}{L} & 0 & \frac{1}{L} & 0 & 0 \\ 0 & 0 & 0 & 0 & 1 & 0 \\ 0 & 0 & 0 & 0 & 0 & 1 \end{bmatrix}$$

The force–deformation relationship is defined at the section level and relates section forces $\mathbf{D}(x)$ with section deformations $\mathbf{d}(x)$, that is, the curvatures $\chi_y(x)$ and $\chi_z(x)$ about the y and z axes, the shear deformations $\gamma_{xy}(x)$ and $\gamma_{xz}(x)$ along the y and z axes, the axial deformation $\varepsilon(x)$, and the torsional deformation $\gamma_t(x)$, respectively. The incremental force–deformation relation states that

$$\Delta\mathbf{D}(x) = \mathbf{k}(x)\Delta\mathbf{d}(x) \tag{2}$$

where $\mathbf{k}(x)$ is the sectional stiffness matrix at the x location along the length L of the element defined as

$$\mathbf{k}(x) = \begin{bmatrix} \sum\limits_{i=1}^{n} E_{it}A_i z_i^2 & -\sum\limits_{i=1}^{n} E_{it}A_i y_i z_i & 0 & 0 & \sum\limits_{i=1}^{n} E_{it}A_i z_i & 0 \\ -\sum\limits_{i=1}^{n} E_{it}A_i y_i z_i & \sum\limits_{i=1}^{n} E_{it}A_i y_i^2 & 0 & 0 & -\sum\limits_{i=1}^{n} E_{it}A_i y_i & 0 \\ 0 & 0 & \frac{dV_y(x)}{d\gamma_{xy}} & 0 & 0 & 0 \\ 0 & 0 & 0 & \frac{dV_z(x)}{d\gamma_{xz}} & 0 & 0 \\ \sum\limits_{i=1}^{n} E_{it}A_i z_i & -\sum\limits_{i=1}^{n} E_{it}A_i y_i & 0 & 0 & \sum\limits_{i=1}^{n} E_{it}A_i & 0 \\ 0 & 0 & 0 & 0 & 0 & \frac{dT(x)}{d\gamma_t} \end{bmatrix}$$

where n is the number of fibers; E_{it} is the tangent modulus of fibers; A_i is the fiber area; y_i is the distance from fiber centroid to the section reference z axis; z_i is the distance from fiber centroid to the section reference y axis; $dV_y(x)/d\gamma_{xy}$, $dV_z(x)/d\gamma_{xz}$, and $dT(x)/d\gamma_t$ represent the shear stiffness in the y, z, and torsion directions.

The section flexibility matrix $\mathbf{f}(x)$ is obtained through inversing the section stiffness matrix $\mathbf{k}(x)$, and the incremental force–deformation equation at the section level is also stated as

$$\mathbf{f}(x) = \mathbf{k}^{-1}(x) \tag{3}$$

$$\Delta\mathbf{d}(x) = \mathbf{f}(x)\Delta\mathbf{D}(x) \tag{4}$$

The final compatibility equation can be established according to the principle of virtual forces, which takes the form

$$\delta(\mathbf{Q})^{\mathrm{T}}\mathbf{q} = \int_0^L \delta(D(x))^{\mathrm{T}}\mathbf{d}(x)dx \tag{5}$$

After substituting Eqs. (1)–(4) in Eq. (5), and after eliminating the $\delta(\mathbf{Q})^{\mathrm{T}}$ on the basis of arbitrary argument, the element compatibility equation is also written as

$$\Delta\mathbf{q} = \left(\int_0^L \mathbf{b}(x)^{\mathrm{T}}\mathbf{f}(x)\mathbf{b}(x)dx \right)\mathbf{Q} = \mathbf{F}\Delta\mathbf{Q} \tag{6}$$

where $\Delta\mathbf{q}$ is the increment of the element node displacement vector and $\mathbf{F}$ is the element flexibility matrix. It should be noted that the aforementioned equations are formally identical to those of the classic FBFE, but the element force interpolation function $\mathbf{b}(x)$ and element flexibility matrix $\mathbf{F}$ couple the shear with the axial and bending responses at the element level.

To calculate the element resisting forces $\mathbf{Q}$, the element needs to be subdivided into several integration points (or monitor sections) along its length L and Gauss–Lobatto quadrature method is adopted to integrate the flexibility matrix $\mathbf{F}$. Each of monitor sections is in turn discretized in several inelastic fibers, and section resisting forces $\mathbf{D}_R(x)$ can be obtained through integrating the fiber stresses over the section. Different from the formulations of the displacement-based fiber elements, the element force determination of the FBFE is not straightforward and requires an iteration algorithm that has been developed by Spacone et al. (1996). In this work, another state determination for shear at the section and element levels must be carried out. The iteration algorithm for axial and bending components has been explained elsewhere (Spacone et al. 1996), and the completed algorithm associated with axial, bending, and shear deformations is presented in Fig. 3.
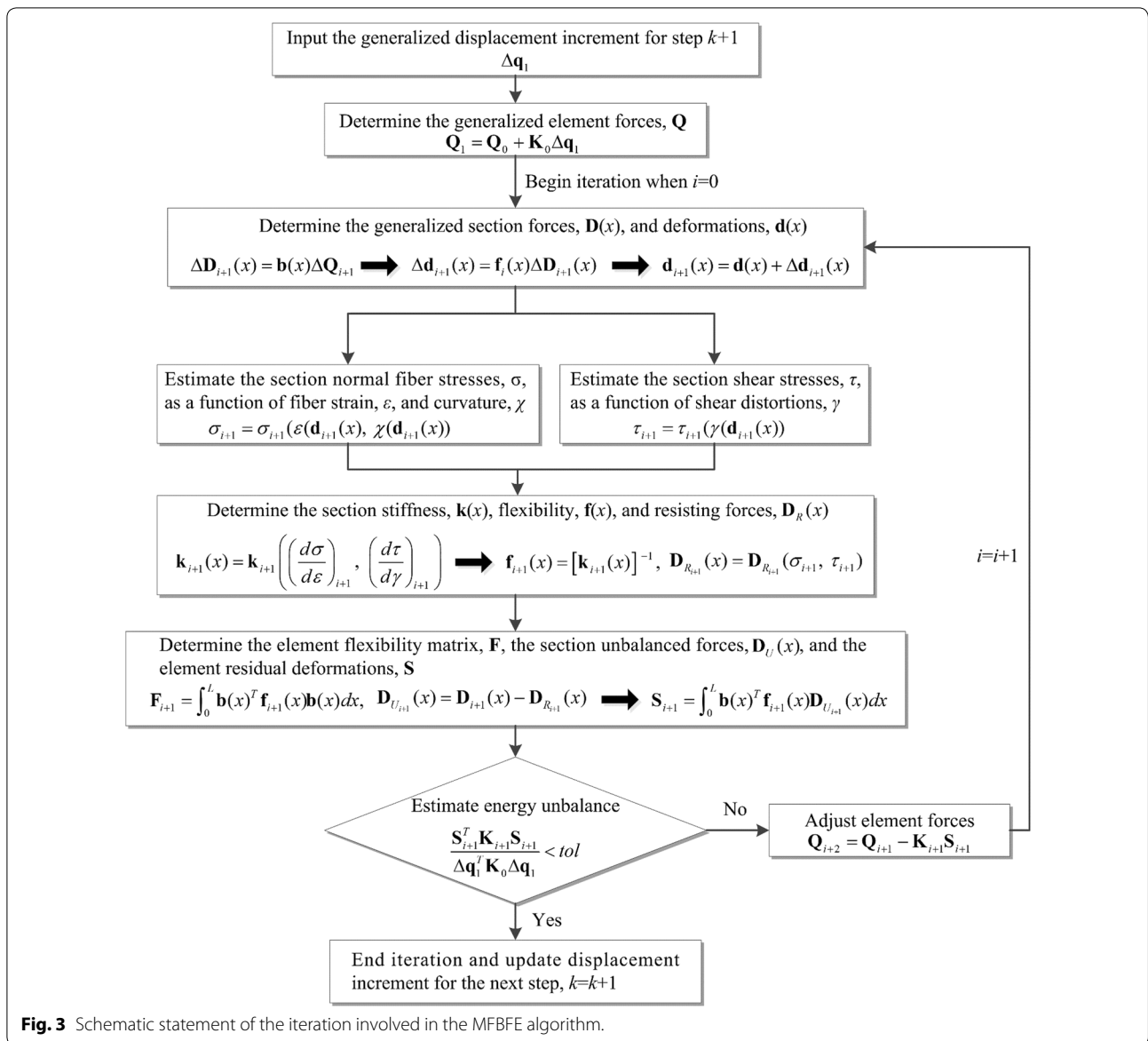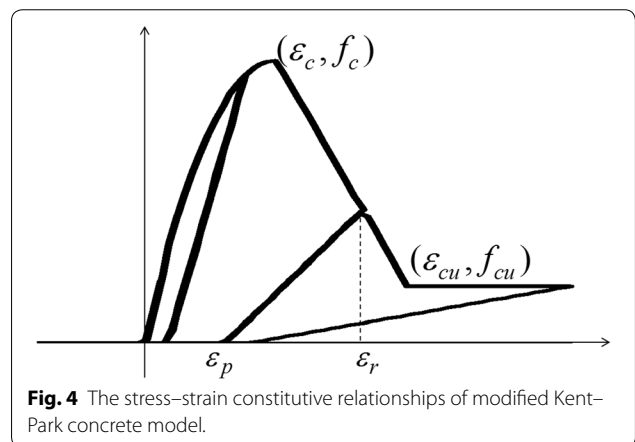
Fig. 3 Schematic statement of the iteration involved in the MFBFE algorithm.

Within each of the monitored sections in the MFBFE, concrete and reinforcement fibers are taken into account. The concrete fibers, in turn, are classified as three segments, that is, cover, unconfined, and confined concrete models. For cover and unconfined concrete fibers, the modified Kent and Park model is adopted (Scott et al. 1982). The unload-reload paths of this model are assumed to remain straight lines with ignoring the tension effect of concrete. The cyclic behavior of the concrete model is shown schematically in Fig. 4 where the maximum strength locates at point (ε_c, σ_c) and the beginning point of the residual strength is (ε_{cu}, σ_{cu}). Note that the unconfined concrete fibers have a residual stress $\sigma_{cu} = 0.2\ \sigma_c$, while the cover concrete model has no residual stress due
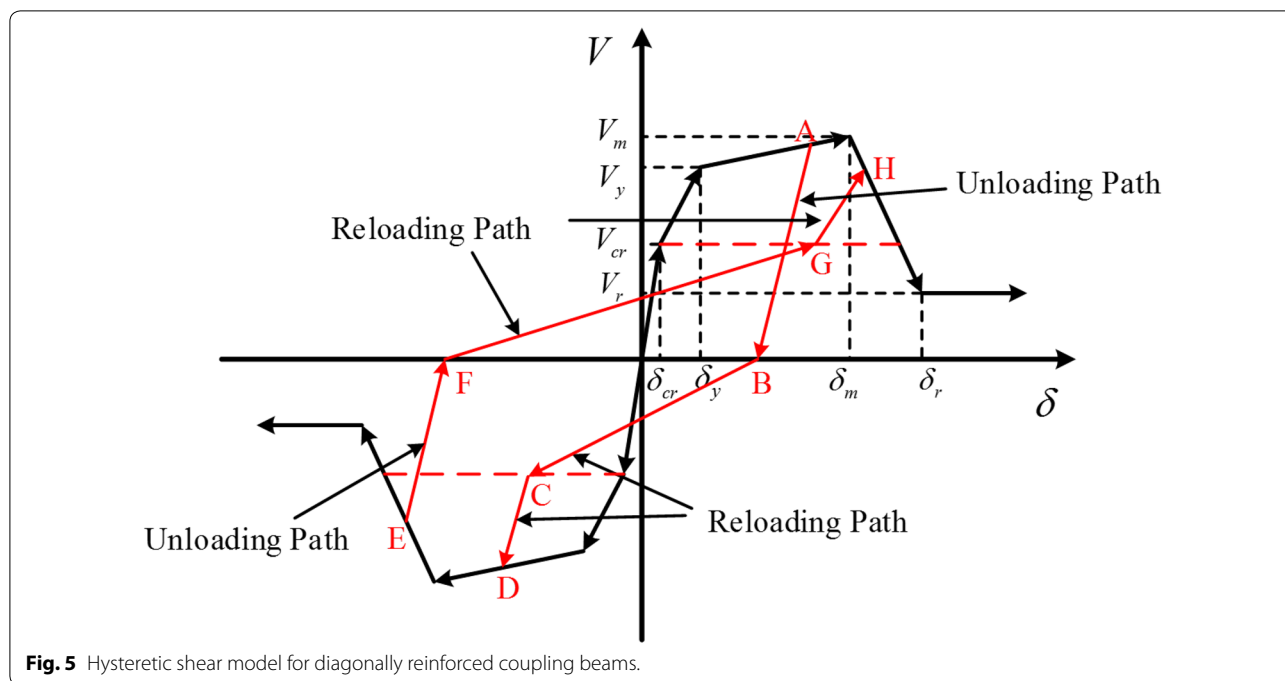

Fig. 4 The stress–strain constitutive relationships of modified Kent–Park concrete model.

Du *et al. Int J Concr Struct Mater*   (2019) 13:34

Page 7 of 26

Fig. 5 Hysteretic shear model for diagonally reinforced coupling beams.

to concrete spalling. For confined concrete fibers, Mander model ([1988](#)) is used to represent the confinement effect of the stirrups. As the behaviors of reinforcement fibers have a great effect on the section response, their model should be selected reasonably so that the behavior characteristics of target structures are able to be exhibited. For this, the Menegotto and Pinto ([1973](#)) allowing for the bar buckling and fracture and Bauschinger effect is chosen to simulate the cyclic behavior of reinforcement fibers. The detailed formulations of the confined concrete and reinforcement models can be found (Mander et al. [1988](#); Menegotto and Pinto [1973](#)).

3 Fomulation and Validation of the MFBBE

The MFBBE is formulated by integrating a MFBFE and a shear model for diagonally reinforced coupling beams. The MFBFE has been introduced in the previous section. The shear model will be introduced in this section. The shear response of diagonally reinforced coupling beams is simulated using a nonlinear V-γ constitutive law. Considering the specified behavior characteristics of diagonally reinforced coupling beams (e.g., stiffness and strength degradation, and pinching effect induced by nonlinear shear deformations), the hysteretic model needs to be reasonably developed to represent its shear response. For diagonally reinforced coupling beams, the four nonlinear phases corresponding to concrete cracking, longitudinal bars yielded, maximum shear capacity, and ultimate shear failure are experienced during the loading history. The backbone curve of the hysteretic model, therefore,

should be determined using four control points in a single load direction so as to describe the nonlinear behavior characters of diagonally reinforced coupling beams, and the hysteretic rules should exhibit the effect of pinching, strength and stiffness deterioration.

3.1 Determination of the Shear Model for Diagonally Reinforced Coupling Beams

To simulate the pinching, strength and stiffness deterioration caused by the shear deformation of diagonally reinforced coupling beams, a simple but accurate hysteretic model is proposed in this section to represent its shear response. The predicted idealization of a load-deformation history using this hysteretic model is shown in Fig. 5. The backbone is multi-linear including cracking, yielding, maximum, and failure points, and the unloading–reloading path is tri-linear. The first step is determining the backbone curve, which is shown as follows. It is worth noting that the control points in the backbone curve in the positive and negative directions are symmetric.

3.2 Determination of Shear Force at the Cracking Point

The modification of Wallace ([2007](#)) to the ASCE 41-06 backbone curve was added a cracking point in load–displacement relationship. Figure 6 is the simplified calculation diagram of cross-section of diagonally reinforced coupling beams. The whole of the component is in an elastic state before concrete cracks. Assuming that longitudinal reinforced bars, diagonal reinforced bars,
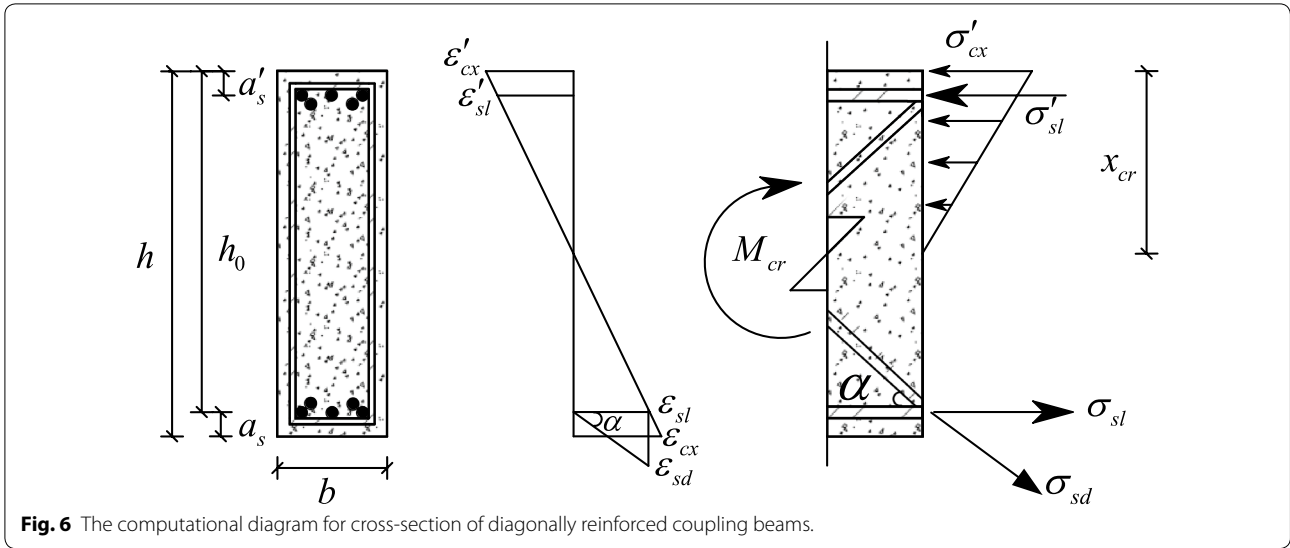
Du *et al. Int J Concr Struct Mater*   (2019) 13:34

Page 8 of 26

Fig. 6 The computational diagram for cross-section of diagonally reinforced coupling beams.

stirrups, and concrete are robustly anchored, and that the centroids of diagonal and longitudinal bars are consistent and bar-slip is neglected, the equations below can be expressed according to compatibility condition at the longitudinal bars.

$$\varepsilon_{sd} \cos \alpha = \varepsilon_{sl} = \varepsilon_t \tag{7}$$

Given $\varepsilon_{sd} = \frac{\sigma_{sd}}{E_{sd} \cos \alpha}$, $\varepsilon_{sl} = \frac{\sigma_{sl}}{E_{sl}}$, and $\varepsilon_t = \frac{\sigma_t}{E_c}$, the stress relation between longitudinal and diagonal bars and concrete thus can be written as follows:

$$\sigma_{sl} = E_{sl} \varepsilon_{sl} = E_{sl} \varepsilon_t = \frac{E_{sl}}{E_c} \sigma_t \tag{8}$$

$$\sigma_{sd} = E_{sd} \varepsilon_{sd} = \frac{E_{sd} \varepsilon_t}{\cos \alpha} = \frac{E_{sd}}{E_c \cos \alpha} \sigma_t \tag{9}$$

When the cross-section cracks, the edge strain of concrete at the tensile side is equal to the limit tensile strain of concrete, that is, $\varepsilon_{cx} = \varepsilon_{tu}$. The section curvature keeps constant under the condition of cross-sections remain plan and normal to the deformed longitudinal axis. According to the compatible condition, the strains of longitudinal and diagonal bars can be calculated by the following equations.

Section curvature:

$$\chi_{cr} = \frac{\varepsilon_{tu}}{h - x_{cr}} \tag{10}$$

Strain of longitudinal bars:

$$\varepsilon_{sl} = \chi_{cr}(h_0 - x_{cr}) \tag{11}$$

Stress of longitudinal bars:

$$\sigma_{sl} = E_{sl} \varepsilon_{sl} = \frac{E_{sl} \varepsilon_{tu}}{h - x_{cr}}(h_0 - x_{cr}) \tag{12}$$

Strain of diagonal bars:

$$\varepsilon_{sd} = \frac{\varepsilon_{sl}}{\cos \alpha} = \frac{\chi_{cr}(h_0 - x_{cr})}{\cos \alpha} \tag{13}$$

Stress of diagonal bars:

$$\sigma_{sd} = E_{sd} \varepsilon_{sd} = \frac{E_{sd} \varepsilon_{tu}}{(h - x_{cr}) \cos \alpha}(h_0 - x_{cr}) \tag{14}$$

As $\varepsilon_{tu} = 2\varepsilon_{t0}$ and $f_t = E_c \varepsilon_{to}$, Eqs. (6) and (8) can be also written respectively as follows:

$$\sigma_{sl} = \frac{2f_t E_{sl}}{E_c(h - x_{cr})}(h_0 - x_{cr}) \tag{15}$$

$$\sigma_{sd} = \frac{2f_t E_{sd}}{E_c(h - x_{cr}) \cos \alpha}(h_0 - x_{cr}) \tag{16}$$

In the same way, the edge stress of concrete at the compressive side can be also determined, which is written by:

$$\sigma'_{cx} = E_c \varepsilon_{tu} = 2f_t \tag{17}$$

As is shown in Fig. 3, the component is in an elastic state before the section cracks, so the stress is triangular distribution along the section depth. The height of compressive concrete is: $x_{cr} = 0.5 \, h$. Ignoring the tensile effect of concrete, taking the moment from the tensile longitudinal bars to compressive longitudinal bars, the moment equation at the crack point can be expressed by:

$$M_{cr2} = n_1 \sigma_{sl} A_{sl}(h_0 - a'_s) + n_2 \sigma_{sd} A_{sd}(h_0 - a'_s)$$
$$\times \cos \alpha - \sigma'_{cx} \frac{bx_{cr}}{2}\left(\frac{x_{cr}}{3} - a'_s\right) \tag{18}$$

Substitution of Eqs. (15–17) in Eq. (18), the moment equation at the cracking point is written as

$$M_{cr2} = \frac{4n_1 f_t E_{sl} A_{sl}}{hE_c}(h_0 - 0.5h)(h_0 - a'_s)$$
$$+ \frac{4n_2 f_t E_{sd} A_{sd}}{hE_c}(h_0 - 0.5h)(h_0 - a'_s) \quad (19)$$
$$- \frac{f_t b h}{2}\left(\frac{h}{6} - a'_s\right)$$

As $M_{cr1} = M_{cr2}$, the shear force at the crack point is given by

$$V_{cr} = \frac{M_{cr1} + M_{cr2}}{L} \quad (20)$$

where ε_{sl} indicates the strain of longitudinal bar; ε_{sd} indicates the strain of diagonal bar; ε_t indicates the tensile strain of the concrete at the tensile longitudinal bar; σ_{sl} indicates the stress of longitudinal bar; σ_{sd} indicates the stress of diagonal bar; σ_t indicates the tensile stress of concrete at the tensile longitudinal bar; E_{sl} indicates the elastic modulus of tensile longitudinal bar; E_{sd} indicates the elastic modulus of tensile diagonal bar; E_c indicates the elastic modulus of concrete; ε_{tu} indicates the limit tensile strain of concrete; ε_{t0} indicates the tensile strain of concrete where the tensile stress is f_t; A_{sl} indicates the area of single longitudinal bar; A_{sd} indicates the area of single diagonal bar; n_1 indicates the number of unilateral tensile longitudinal bars; n_2 indicates the number of unilateral tensile diagonal bars; α indicates the angle between longitudinal and diagonal bars.

3.3 Determination of Shear Displacement at the Cracking Point

For rectangular section, the shear stress is parabolic distribution along the section y direction. The component is considered as an elastic solid before the concrete cracks. The average shear distortion at the cracking point therefore is given by

$$\gamma_{cr} = k\frac{V_{cr}}{G_c A} \quad (21)$$

So, the shear displacement can be written as follows.

$$\delta_{cr} = \gamma_{cr} L = k\frac{V_{cr} L}{G_c A} \quad (22)$$

where V_{cr} indicates the shear force at the cracking point; δ_{cr} indicates the shear displacement at the cracking point; $G_c = E_c/2(1 + u)$ indicates the shear modulus of concrete, u is Poisson's ratio; A indicates the cross-section area; L indicates the span of the component; k is equal

to 1.2 for a rectangular section, indicating the sectional modified factor.

3.4 Determination of Shear Force at the Yielding Point

The component begins to enter into yielding phase when the longitudinal bars of diagonally reinforced coupling beams reach yielding strength. As is shown in Fig. 7, the influence of longitudinal and diagonal bars on the component reaching the yielding stage is obvious, while Hindi and Hassan (2004) note that contribution of concrete core to the diagonal compression force could be noticeable since the concrete compressive strength is usually quite high in coupled wall systems. The diagonal compression is carried by the diagonal reinforcement and the concrete core surrounded by the diagonal bars in that direction, while the diagonal tension is carried only by the diagonal reinforcement. The detailed calculation process is shown below.

Assuming that the centroids of diagonal and longitudinal bars are coincidence, and taking moment from the tensile reinforcements including longitudinal and diagonal bars, the sectional yielding moment in tension therefore can be derived as follows

$$M_{y1} = \left(n_1 f_{yl} A_{sl} + n_2 \sigma_{sd} A_{sd} \cos\alpha\right)\left(h - a_s - a'_s\right). \quad (23)$$

Following the same way, the yielding moment in compression can be also derived by taking moment from the compression reinforcements including longitudinal and diagonal bars and the concrete core surrounded by the diagonal bars,

$$M_{y2} = \left(n_1 f'_{yl} A_{sl} + n_3 \sigma'_{sd} A'_{sd} \cos\alpha + f_c A_c\right)\left(h - a_s - a'_s\right) \quad (24)$$

The yielding shear force therefore can be easily obtained by the following equation:

$$V_y = \frac{M_{y1} + M_{y2}}{L} \quad (25)$$

where f_{yl}, f'_{yl} indicates the yield strength of longitudinal bar; σ_{sd} indicates the stress of diagonal bar, which can be computed by the equation: $\sigma_{sd} = \xi f_{yd}$, ξ indicates the strength reduction factor; A_{sd} indicates the area of single tensile diagonal bar; A'_{sd} indicates the area of single compressive diagonal bar; n_1 indicates the number of unilateral longitudinal bars; n_2 indicates the number of tensile diagonal bars; n_3 indicates the number of compressive diagonal bars, f_c indicates the compression strength of concrete core surrounded by the diagonal bars, A_c indicates the area of concrete core.
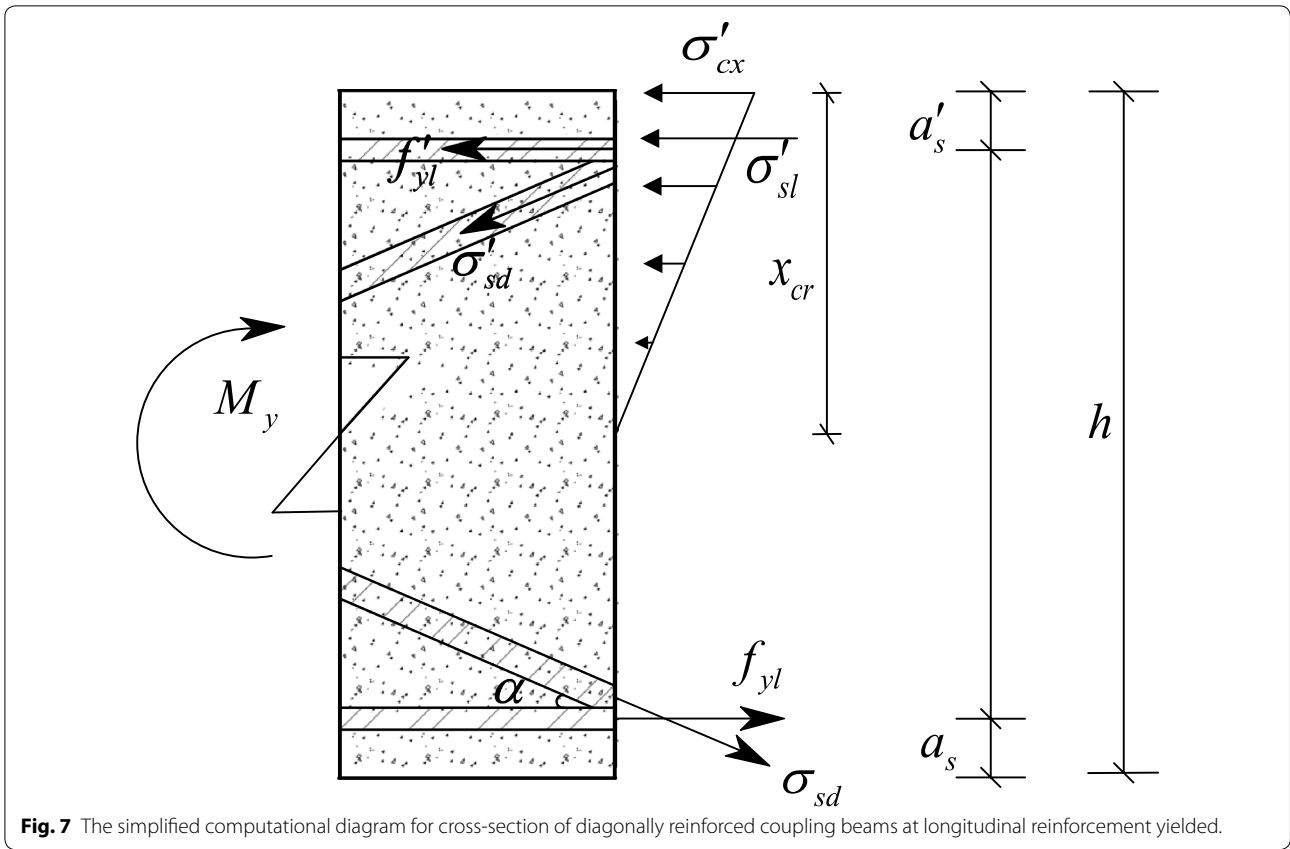
Du *et al. Int J Concr Struct Mater*   (2019) 13:34

Page 10 of 26

Fig. 7 The simplified computational diagram for cross-section of diagonally reinforced coupling beams at longitudinal reinforcement yielded.

3.5 Determination of Shear Displacement at the Yielding Point

Assuming that longitudinal bars, stirrups, and diagonal bars are all able to interact with concrete well, and that these components all meet the requirement of compatibility condition, the average shear distortion can be expressed through strain relationship of plane.

$$\gamma_{xy} = \varepsilon_x + \varepsilon_y - 2\varepsilon_{45°} \tag{26}$$

When longitudinal bars of diagonally reinforced coupling beams begin to yield, the component reaches the yielding phase. The horizontal strain of the component is given by

$$\varepsilon_x = \varepsilon_{sl} = f_{yl}/E_{sl} \tag{27}$$

The vertical strain is expressed by

$$\varepsilon_y = \varepsilon_{st} = \sigma_{st}/E_{sl} \tag{28}$$

The shear force acted on the component at this time is equal to yielding shear force V_y. Assuming that V_y is mainly carried by diagonal bars and stirrups, the expression of V_y can be easily obtained through summation of forces in the y-direction.

$$V_y = (n_2 + n_3)\sigma_{sd}A_{sd}\sin\alpha + 2n\sigma_{st}A_{st} \tag{29}$$

The stress–strain of concrete in the direction of principal compressive stress follows linear relation due to the principal compressive stress of concrete less than its peak stress. Assuming that the angle direction between principal compressive stress of concrete and stirrups or longitudinal bars is 45°, the strain at the 45° is:

$$\varepsilon_{45°} = \sigma_2/E_c \tag{30}$$

Ignoring the influence of principal tensile stress of concrete, as the shear stress acted on the component is τ_y, the equation below can be easily obtained by the planar stress relationship.

$$\tau_y = -\sigma_2/2 \tag{31}$$

Substitution of Eqs. (27–30) in Eq. (26), the average shear distortion at the yielding point can be written as

$$\gamma_y = \frac{f_{yl}}{E_{sl}} + \frac{\sigma_{st}}{E_{st}} + \frac{4\tau_y}{E_c} \tag{32}$$

Therefore, the shear displacement at the yielding point can be easily derived

$$\delta_y = \gamma_y L \tag{33}$$

where $\tau_y = 1.2V_y/bh_0$ indicates the average yielding shear stress of rectangular section; σ_{st} indicates the stress of

stirrups when longitudinal bars reaches yielding strength; σ_2 indicates the principal compressive stress of concrete when longitudinal bars reaches yielding strength; E_{st} indicates the elastic modulus of stirrups; E_{sl} indicates the elastic modulus of longitudinal bars; n indicates the number of stirrups; A_{st} indicates the area of single limb stirrup; other symbols are the same as previous chapters.

3.6 Determination of Shear Force at the Maximum Point

When the diagonal and longitudinal bars of diagonally reinforced coupling beams both reach yielding strength, as is shown in Fig. 7, at this time $\sigma_{sd} = f_{yd}$, $\sigma'_{sd} = f'_{yd}$, the component reaches the maximum shear capacity. Assuming that the maximum shear force acted on the component is mainly carried by diagonal, longitudinal bars, and concrete core. Taking moment from the tensile reinforcements including longitudinal and diagonal bars to the compressive reinforcements, the equation for the sectional maximum moment in tensile is expressed as follows

$$M_{m1} = \left(n_1 f_{yl} A_{sl} + n_2 f_{yd} A_{sd} \cos\alpha\right)(h - a_s - a'_s). \tag{34}$$

In the same way, the sectional maximum moment in compression can be easily derived by taking moment from the compression reinforcements including longitudinal and diagonal bars and the concrete core surrounded by the diagonal bars,

$$M_{m2} = \left(n_1 f'_{yl} A_{sl} + n_3 f'_{yd} A'_{sd} \cos\alpha + f_c A_c\right)(h - a_s - a'_s) \tag{35}$$

Thus, the maximum shear force can be calculated by the following equation.

$$V_m = \frac{M_{m1} + M_{m2}}{L} \tag{36}$$

where f_{yd} indicates the yielding strength of tensile diagonal bar; f'_{yd} indicates the yield strength of compressive diagonal bar; other symbols are the same as above.

3.7 Determination of Shear Displacement at the Maximum Point

Gerin and Adebar (2004) built a relationship between average yielding shear distortion and average maximum shear distortion through regression analyses of experimental data of 21 membrane elements subjected to reversed shear force. This equation is shown below.

$$\frac{\gamma_m}{\gamma_y} = 4 - 12\frac{\tau_y}{f_c} \tag{37}$$

where $\tau_y \leq 0.25 f_c$, this is to prevent the concrete from shear failure before reinforcements reach its yielding strength.

The equation described above herein is adopted to calculate the shear displacement at the maximum point, which can be easily obtained by:

$$\delta_m = \gamma_m L = \left(4 - 12\frac{\tau_y}{f_c}\right)\gamma_y L \tag{38}$$

3.8 Determination of Failure Point

As the experimental tests associated with the diagonally reinforced coupling beams subjected to reversed cyclic loading in the literatures are generally terminated before component shear strength dropped significantly, the residual strength for the backbone curve at the failure point thus is hard to identify. The residual shear strength here is defined as the 0.2 V_m. To determine the shear displacement at the failure point, the stiffness of softening branch should be identified. Gong and Fang (1988a, b) determined the equation used for calculating the softening branch stiffness of coupling beams through regression analyses of experimental data of 15 RC coupling beams specimens subjected to reversed cyclic loading tests. Herein, the softening stiffness equation proposed by Gong and Fang (1988b) is adopted to calculate the shear displacement at the failure point, which is shown below.

$$K_g = -\frac{1}{6}\beta\sqrt{\tau_0}K_y$$

where β is the ratio of residual shear force to maximum shear force; τ_0 is the ratio of nominal shear stress to concrete strength; K_y is the tangent stiffness at yield.

3.9 Determination of Hysteretic Rules

Figure 5 shows a typical reversed shear cycle. The loading starts in the positive load direction and follows the backbone curve for the unload-reload paths described in the previous section when the crack shear force is not reached. Once the crack shear force is exceeded, at point A the load direction is reversed. Unloading from point A follows a straight line shooting for point B whose coordinates are (0.85 δ_A, 0) according to the reference (Said et al. 2005). As loading continues in the negative direction, a significant reduction in the tangent stiffness occurs and this allows for the pinching effect experienced by non-slender RC structures under reversed-cyclic loading. Loading in the negative direction proceeds until point C (0.85 δ_D, V_{cr}) is reached and the loading path is changed and leads the response to point D, at which loading in the negative direction follows the negative backbone curve. As the loading is re-reversed at point E,

Table 1 Design parameters.

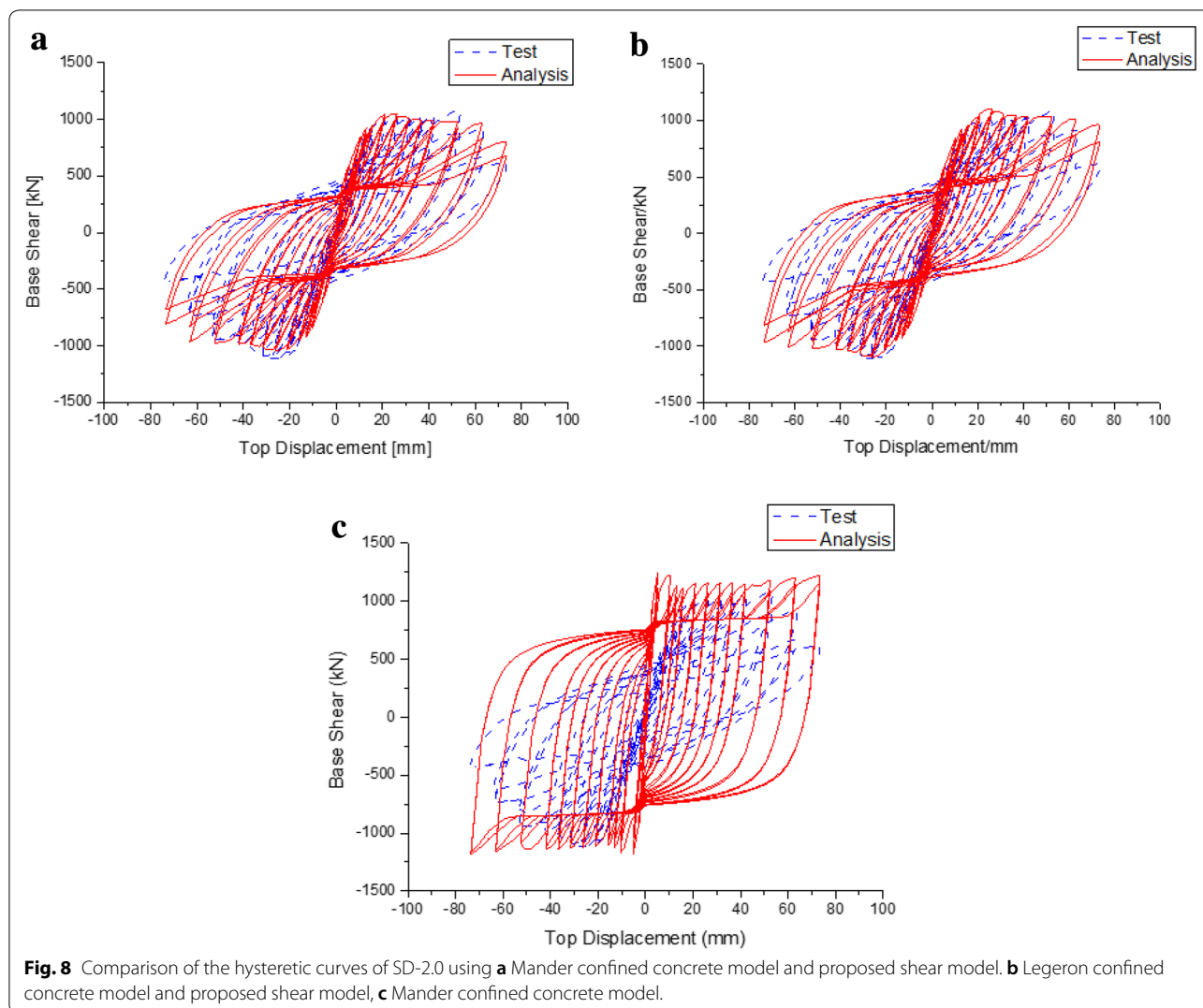| Specimen	Lequesne et al. (2012)		Han et al. (2015)	
	CB-1	CB-2	SD-2.0	BD-2.0
f_c', MPa	41	41	40	40
f_y (longitudinal reinforcement), Mpa	430	440	506	506
f_y (ties), Mpa	525	475	506	506
f_y (diagonal reinforcement), Mpa	430	430	438	438
f_u (diagonal reinforcement), Mpa	680	680	587	587
b (beam width), mm	150	150	250	250
h (beam height), mm	600	600	525	525
L (beam length), mm	1050	1050	1050	1050
ρ_d (diagonal bars ratio), %	1.11	1.11	2.35	2.35
ρ_s (stirrup ratio), %	1.24	1.43	2.84	2.43
ρ_l (longitudinal bars ratio), %	1.9	1.9	1.42	1.42
α, degree	24.6	24.6	20.4	22.1
Span–depth ratio, L/h	1.75	1.75	2.0	2.0

the unloading stiffness to point F (0.85 δ_E, 0) is calculated in the same way as for the positive direction. After point F, positive loading continues with a reduced stiffness calculated based on the coordinates of point H until the positive reloading branch is reached at point G (0.85 δ_H, V_{cr}). Reloading then follows that of the previous reloading branch until the positive backbone curve is reached.

3.10 Model Evaluation and Validation

To validate the efficiency and accuracy of the proposed MFBBE in simulating the nonlinear response of diagonally reinforced coupling beams, 4 components specimens subjected to reversed cyclic loading tested by Lequesne et al. (2012) and Han et al. (2015) are chosen as the simulation objects. The detailed design information about these 4 specimens is summarized in Table 1. In the process of building the FE model of diagonally reinforced coupling beams, there are many factors that can influence the reliability and accuracy of analytical results, such as the number of fibers in the section and the confinement effect of the stirrups. Specifically, it is confirmed that the plastic deformation capacity of RC members can be effectively improved by considering the confinement effect of the stirrups (Mander et al. 1988; Legeron and Paultre 2003). Although numerous stirrup-confined concrete models are available, further verification through comparison with the experimental data is required to determine the most appropriate model for simulating RC coupling beams subjected to reversed cyclic loading.

Given the abovementioned requirements, the Mander et al. (1988) and Legeron and Paultre (2003) confined concrete models are compared using SD-2.0 as an example. Concrete and reinforcing steels are respectively

simulated with the corresponding models introduced in the Sect. 2. The modeling strategy is that the SD-2.0 specimen is modeled using a single MFBFE with five Gauss–Lobatto integration points (i.e., monitored sections). Besides, the additional section with assigning the proposed shear model is also attached to each of these five monitored sections to simulate the shear response. A comparison between the experimental data and the simulation results using different confined concrete models is presented in Fig. 8a, b. Figure 8a demonstrates that the predicted backbone curve and hysteresis loops using the Mander model are compared to the test data with closer agreement. In contrast, the results shown in Fig. 8b simulated by Legeron model somewhat underestimate the softening speed and overestimate the ductility. To examine the influence of nonlinear shear deformation on the diagonally reinforced coupling beams, another modeling scheme that the SD-2.0 is solely simulated using a single FBFE with classical fiber model and without attaching the extra shear model is taken into account. The cover and unconfined concrete and reinforcing bars are simulated using the same models as the MFBBE used. The confined concrete model is simulated using Mander model. The simulation result is compared in Fig. 8c showing an apparent discrepancy in both predicted backbone curve and hysteretic loop. This implies that the nonlinear shear deformation has a great effect on the total lateral displacement, and that the classical fiber model fails to exhibit these nonlinear behavior characteristics of diagonally reinforced coupling beams in simulating pinching effect, strength and stiffness deterioration. Here we note that because the element shear and flexural forces are coupled in MFBFE, flexural and shear deformation

Fig. 8 Comparison of the hysteretic curves of SD-2.0 using **a** Mander confined concrete model and proposed shear model. **b** Legeron confined concrete model and proposed shear model, **c** Mander confined concrete model.

cannot be separated independently in analysis. Based on the above simulation of SD-2.0, it can be concluded that the accuracy of the simulation results for diagonally reinforced coupling beams relies largely on the employment of the proposed shear model. The different confined concrete models, on the other hand, have slight influence on the accuracy of the predicted results.

Based on this validation, the proposed MFBBE associated with the modeling strategy using Mander confined concrete model is adopted to simulate all of the rest specimens presented in Table 1. The comparisons between the experimental data and simulation results are shown in Fig. 9. Good agreements are also achieved for all of these specimens. This outcome confirms that the strength deterioration and pinching observed in the tests can be well captured using the proposed MFBBE. The backbone curve and the hysteretic behavior are also proven to agree well with the experimental data, thus

conclusively validating the efficiency and accuracy of the proposed MFBBE in simulating the nonlinear response of diagonally reinforced coupling beams dominated by the shear deformation.

4 Fomulation and Validation of the MFBWE

The formulation of the MFBWE is formally identical to that of the MFBBE, but the only thing that is different from the MFBBE is the shear model. For RC shear walls, the three stages regarding reinforcement yielded, maximum shear capacity, and ultimate shear failure are considered as the primary nonlinear behavior. Therefore, the most suitable shear model for RC shear walls should have a backbone curve capable of defining three control points and hysteretic rules that can describe the pinching, strength and stiffness deterioration. The Ibarra-Krawinkle Pinching (IKP) material model (Ibarra et al. 2005) that incorporates energy-controlled stiffness and strength
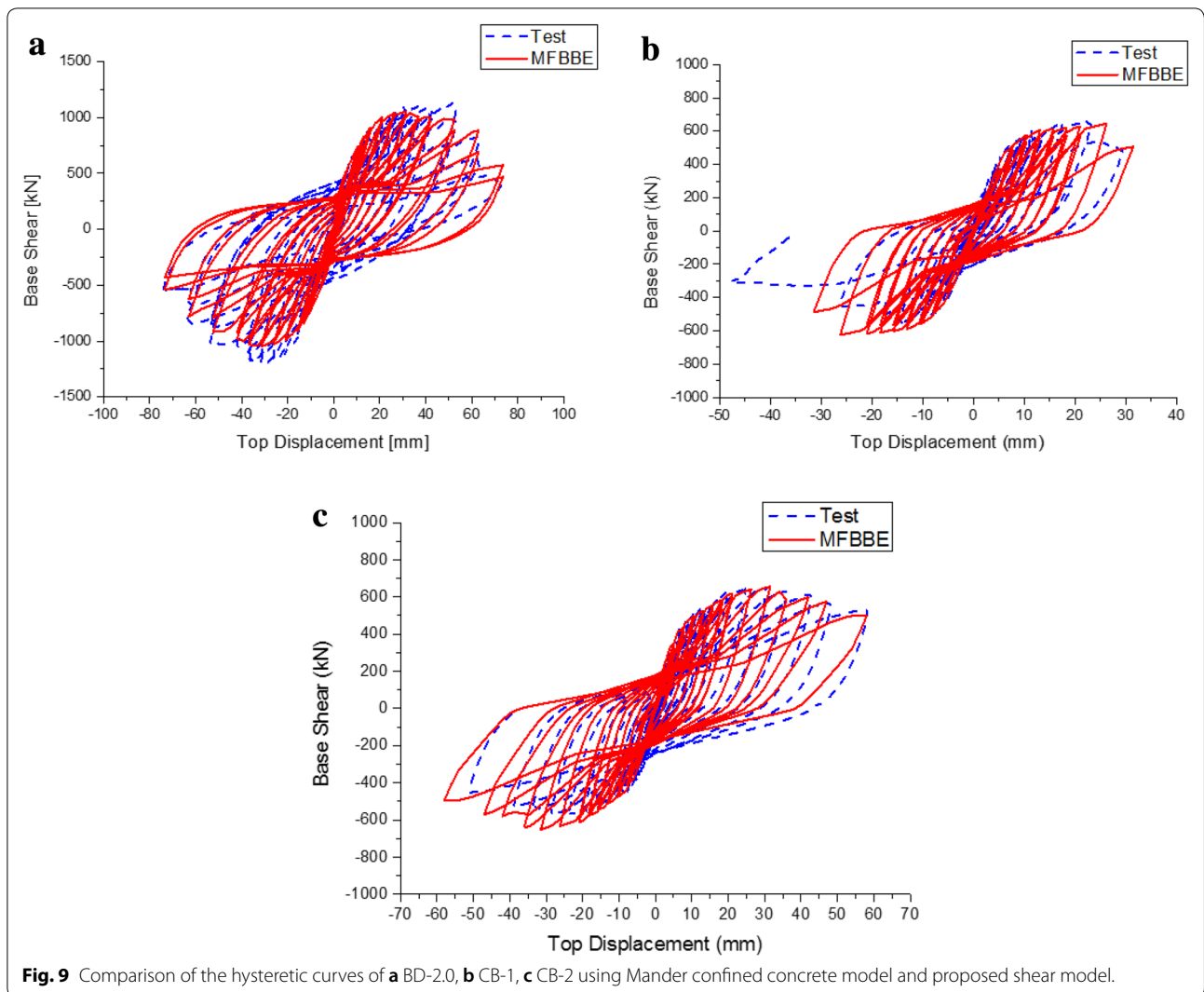
Du *et al. Int J Concr Struct Mater*   (2019) 13:34

Page 14 of 26

Fig. 9 Comparison of the hysteretic curves of **a** BD-2.0, **b** CB-1, **c** CB-2 using Mander confined concrete model and proposed shear model.

deterioration herein is utilized as the shear model of RC shear walls.

To reflect the nonlinear behavior characteristics of RC shear walls, calibration of the IKP model is required. A critical issue for the IKP model is how to determine its backbone curve (Fig. 10). There are numerous analytical models available in the literature that can accurately simulate the nonlinear response of RC shear wall subjected to reversed cyclic loading (Vulcano et al. 1988; Kabeyasawa et al. 1982; Massone et al. 2004, 2009; Kolozvari et al. 2015; Hirosawa 1975; Gulec and Whittaker 2009). The empirical formula proposed by Hirosawa (1975) is usually recommended to calculate the yielding shear force of RC shear wall.

$$V_y = \left[0.0679\rho_t^{0.23}\left(f_c' + 17.6\right)/(M/VL + 0.12)^{0.5}\right]b_ej$$
$$+ \left[0.845\left(f_{wh}\rho_{wh}\right)^{0.5} + 0.1\sigma_0\right]b_ej \quad (39)$$

$$j = \frac{7(L - a/2)}{8} \quad (40)$$

The initial elastic shear stiffness of the wall is defined as

$$K_e = \frac{G_c A_w}{\chi h_w} \quad (41)$$

$$\chi = 3(1 + u)\left[1 - u^2(1 - v)\right]/4\left[1 - u^3(1 - v)\right] \quad (42)$$

The shear displacement at the yielding point thus is given by

$$\delta_y = \frac{V_y}{K_e} \quad (43)$$

where V_y is the yielding shear force; f_c' is the compressive strength of concrete; ρ_t is the effective tensile
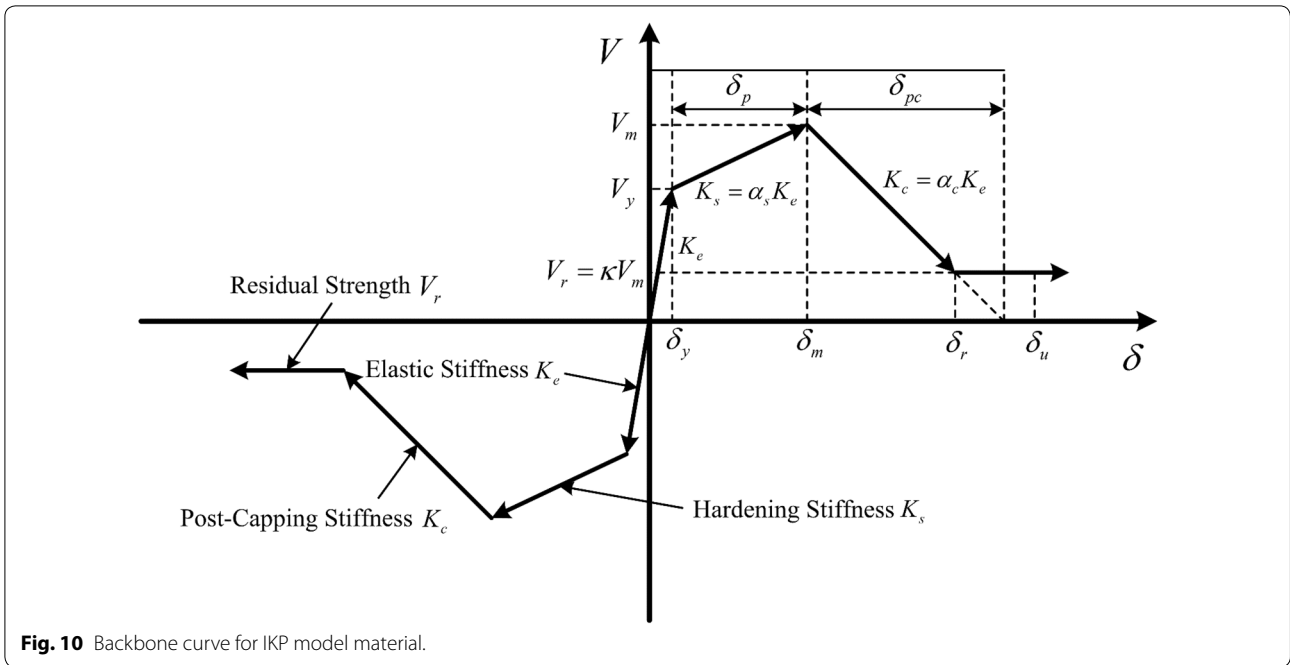
Fig. 10 Backbone curve for IKP model material.

reinforcement ratio; M/VL is the ratio of the shear span to depth; b_e is the width of wall section; f_{wh} is the yield strength of horizontal wall reinforcement; ρ_{wh} is the effective horizontal wall reinforcement ratio; σ_0 is the average stress over entire wall cross section area; A_w is the section area of shear wall; K_e is the initial elastic shear stiffness; G_c is the shear module of concrete; χ is the shape factor for shear deformation, δ_y is the yielding shear displacement, h_w is the wall height; L, a, u, and v are the geometrical parameters that can be found in the literature (Vulcano et al. 1988).

The maximum point can be determined once the maximum shear force and post-yielding shear stiffness are established. As the post-yielding shear stiffness cannot be obtained directly from relevant theory, it must be estimated in terms of experimental data of RC shear walls. Kabeyasawa et al. (1982) suggested an empirical formula to determine the ratio α_s of the stiffness after shear yielding to the initial elastic shear stiffness.

$$\alpha_s = 0.14 + 0.46\rho_{wh}f_{wh}/f_c' \tag{44}$$

$$K_s = \alpha_s K_e \tag{45}$$

The maximum shear-resistant formula is mainly related to the shape of shear wall section, which can be found in the literature (Gulec and Whittaker 2009).

For rectangular walls, the maximum shear capacity is written as

$$V_m = \frac{1.5\sqrt{f_c'}A_w + 0.25F_{vw} + 0.20F_{vbe} + 0.40P}{\sqrt{h_w/l_w}} \tag{46}$$

For symmetric shear-critical walls with boundary elements, the maximum shear capacity equation is defined by

$$V_m = \frac{(0.04f_c')A_t + 0.40F_{vw} + 0.15F_{vbe} + 0.35P}{\sqrt{h_w/l_w}} \tag{47}$$

where V_m is the maximum shear strength, A_t is the gross area for barbell walls and the effective area for flanged walls, F_{vw} is the force provided by vertical web reinforcement, F_{vbe} is the force attributed to vertical boundary element reinforcement, P is the axial force, l_w is the length of wall, other symbols are the same as the contents presented above.

The residual shear strength for the skeleton curve could be difficult to be either estimated in an empirical formula or calibration in experimental data, because the most of quasi-static cyclic tests were terminated in general before the walls shear strength dropped significantly. For the post-capping stiffness K_c, it can be estimated through fitting the experimental data.

The hysteretic rules associated with unload-reload paths, strength and stiffness degradation developed by Ibarra et al. (2005) are utilized herein to represent

Table 2 Properties of concrete.

Concrete type	$f_{cu, 150\,mm}$ (MPa)	$f_{c, 150\,mm}$ (MPa)
C30	20.7	19.7
C40	37.7	30.8

the cyclic response. To verify the accuracy and reliability of the proposed analytical method, 9 RC shear walls specimens tested by Zhang et al. (2007), having different axial compression ratios, aspect ratios, longitudinal bars ratios, concrete strengths, are used as analytical examples. The mechanics properties of concrete and reinforcements as well as the detailed design parameters of these nine RC shear wall specimens are presented in Tables 2, 3, and 4, respectively. The modeling strategy is similar to the diagonally reinforced coupling beams above. When constructing their FE models, each of these nine specimens is simulated using a single MFBFE with five Guass-Lobatto integration points; meanwhile, the P-Delta effect at the element level is also taken into account. At the section level, the validated confined concrete model above (i.e., Mander confined concrete model) is adopted to model the confinement of stirrups, and the cover

concrete and reinforcements are also simulated as same as the MFBBE; besides, an extra sectional constitutive law of shear force versus shear displacement representing the shear behavior of RC shear wall is also added to each of these five integration points. Comparisons between hysteretic curves observed by test and analytical predictions of the lateral load versus wall top displacement are presented in Figs. 11, 12. It can be observed from the Figs. 11, 12 that overall cyclic behavior characteristics of these nine RC shear walls are accurately reflected by the proposed MFBWE, including the hysteretic loop shape of lateral load versus top displacement response, deterioration of unload-reload stiffness, maximum shear force, and moderate pinching behavior, validating that the proposed MFBWE is capable of capturing the nonlinear behavior characteristics of RC shear walls observed from test.

5 Fomulation and Validation of the Cwe

The formulation of the CWE is integrating the MFBBE and MFBWE as shown in Fig. 13. Note that the loading strategy in simulation is identical to that of the test. The modeling scheme is that the RC wall piers and diagonally reinforced coupling beams are simulated using the

Table 3 Properties of reinforcing bars.

Reinforcement type	Φ4	Φ6	Φ8	Φ10	Φ10	Φ12
Diameter (mm)	3.91	6.54	8.05	9.41	9.74	12.55
Yielding strength (MPa)	348	392	343	352	379	325
Ultimate strength (MPa)	409	479	447	493	554	195
Elastic modulus (MPa)	198,800	200,600	206,800	202,700	181,200	169,000

Table 4 Details parameter of specimens.

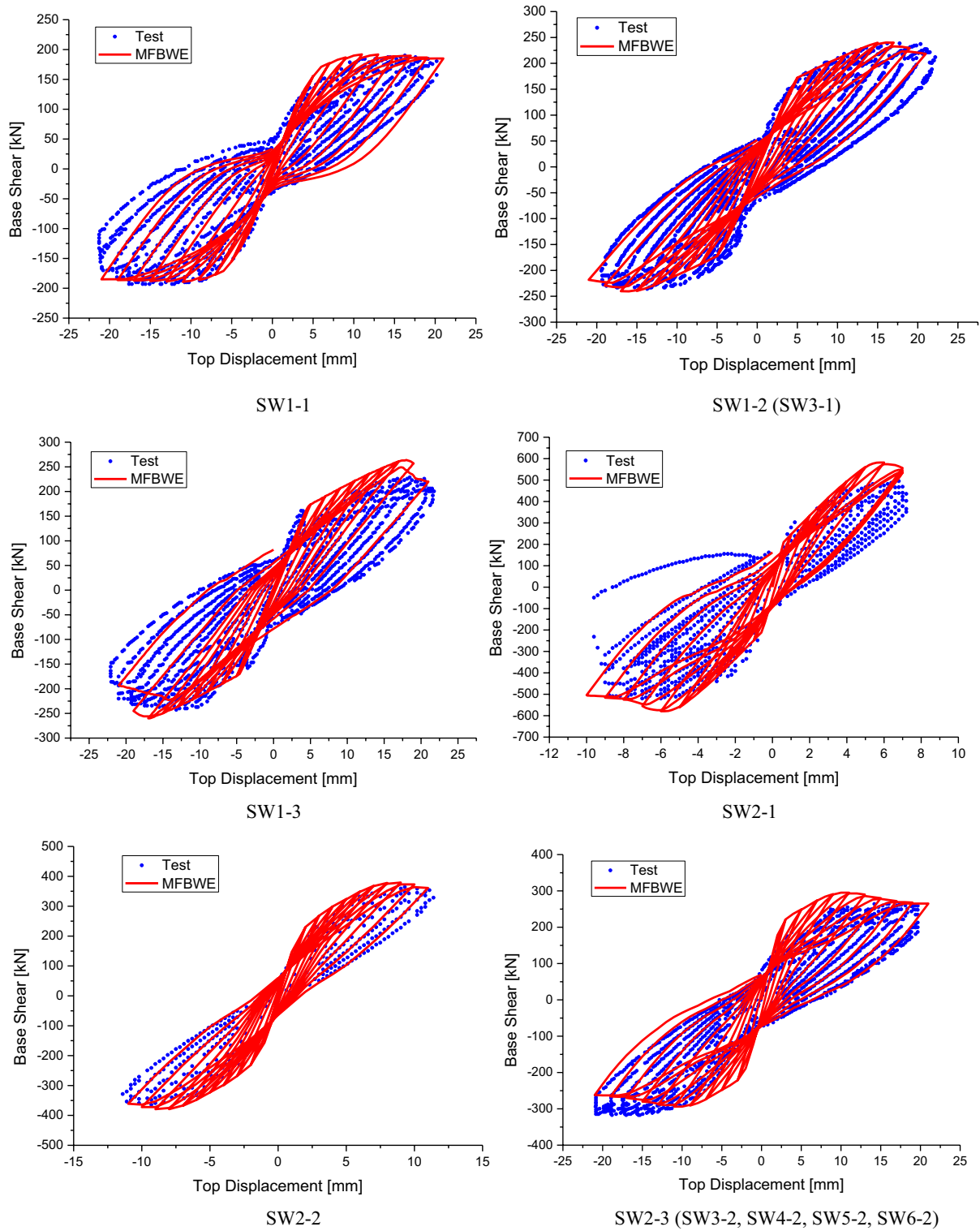| Specimen	Section dimension (mm) (span x depth x width)	Aspect ratio	Concrete strength	Axial compression ratio	Longitudinal bar	Stirrup
SW1-1	2000 × 1000 × 125	2.0	C30	0.1	6Φ10	Φ6@80
SW1-2	2000 × 1000 × 125	2.0	C30	0.2	6Φ10	Φ6@80
SW1-3	2000 × 1000 × 125	2.0	C30	0.3	6Φ10	Φ6@80
SW2-1	1000 × 1000 × 125	1.0	C40	0.3	6Φ10	Φ6@80
SW2-2	1500 × 1000 × 125	1.5	C40	0.3	6Φ10	Φ6@80
SW2-3	2000 × 1000 × 125	2.0	C40	0.3	6Φ10	Φ6@80
SW3-1	2000 × 1000 × 125	2.0	C30	0.2	6Φ10	Φ6@80
SW3-2	2000 × 1000 × 125	2.0	C40	0.3	6Φ10	Φ6@80
SW4-1	2000 × 1000 × 125	2.0	C40	0.3	6Φ8	Φ6@80
SW4-2	2000 × 1000 × 125	2.0	C40	0.3	6Φ10	Φ6@80
SW5-1	2000 × 1000 × 125	2.0	C40	0.3	6Φ10	Φ6@80
SW5-2	2000 × 1000 × 125	2.0	C40	0.3	6Φ10	Φ6@80
SW6-1	2000 × 1000 × 125	2.0	C40	0.3	6Φ10	Φ4@80
SW6-2	2000 × 1000 × 125	2.0	C40	0.3	6Φ10	Φ6@80

Fig. 11 Comparisons between the experimental data and the analytical results using the proposed MFBWE.
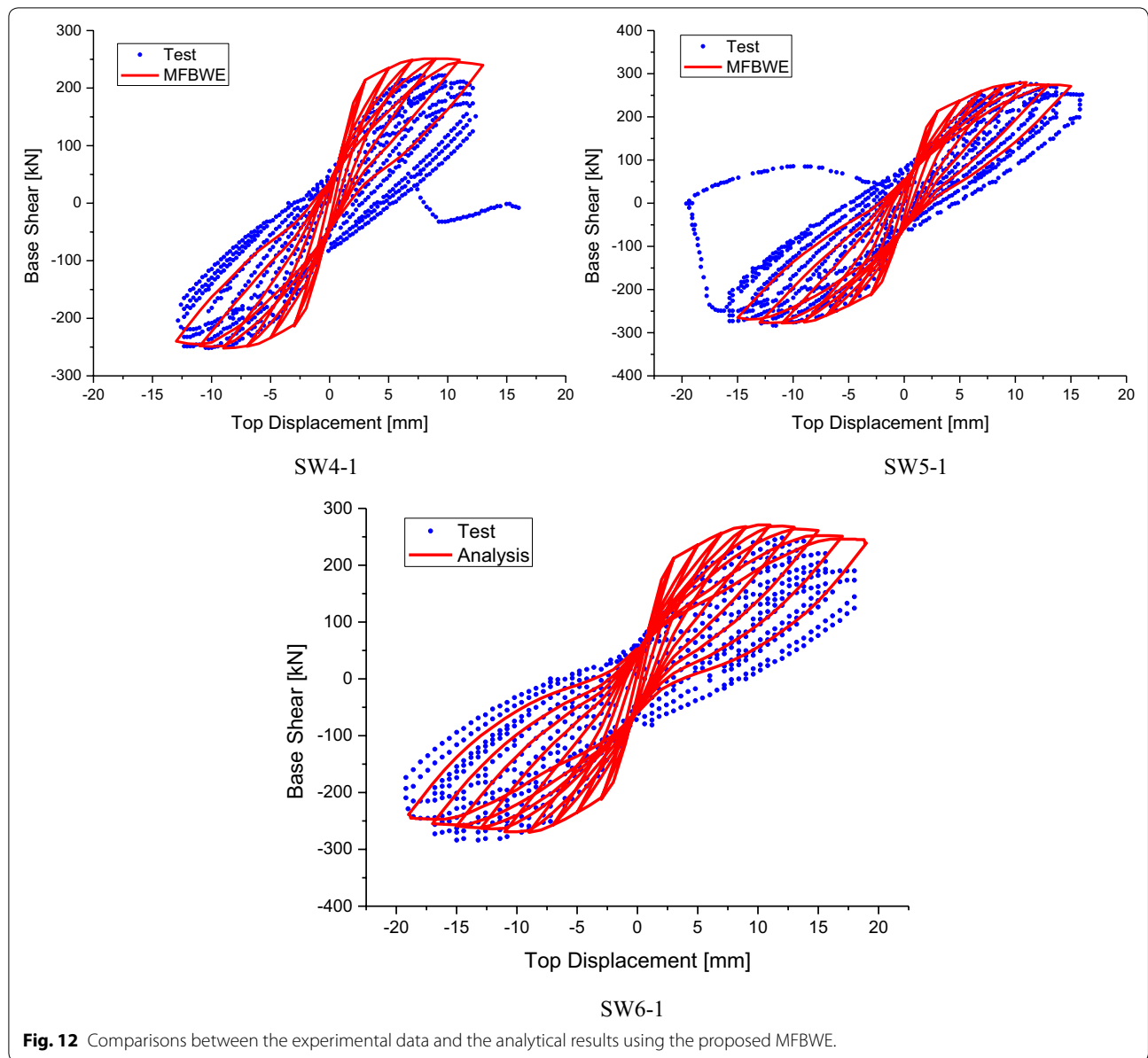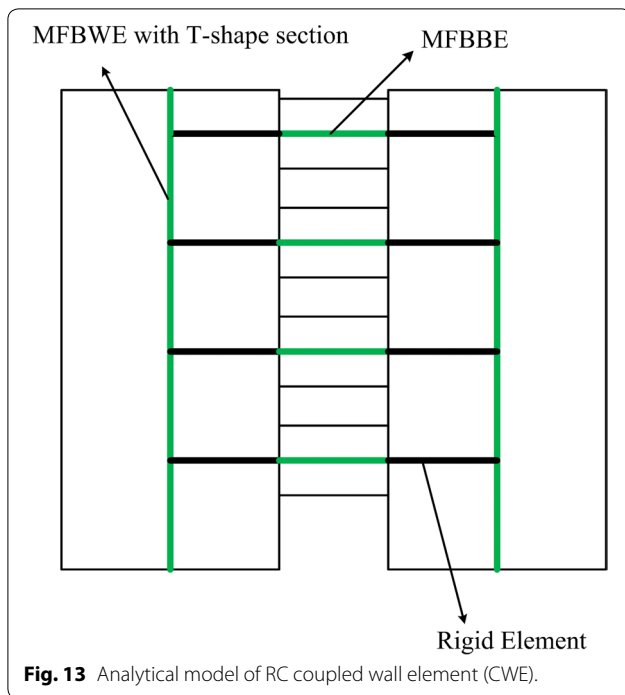
Fig. 12 Comparisons between the experimental data and the analytical results using the proposed MFBWE.

proposed MFBWE and MFBBE models respectively. It is worth noting that the rigid element is employed to connect the shear wall and coupling beam so as to represent the physical size of wall piers. To verify the efficiency and accuracy of the proposed CWE in modeling the nonlinear response of RC coupled walls, two large-scale 4-story RC coupled wall specimens constructed at approximately 1/3 scale (Lequesne et al. 2012) are used as the simulation examples. To account for the consistent with the test, the wall piers are simulated using the proposed MFBWE with a T-shaped section. The two specimens have different properties of concrete and reinforcements, reinforcement ratios, stirrup ratios, and coupling ratios, which can
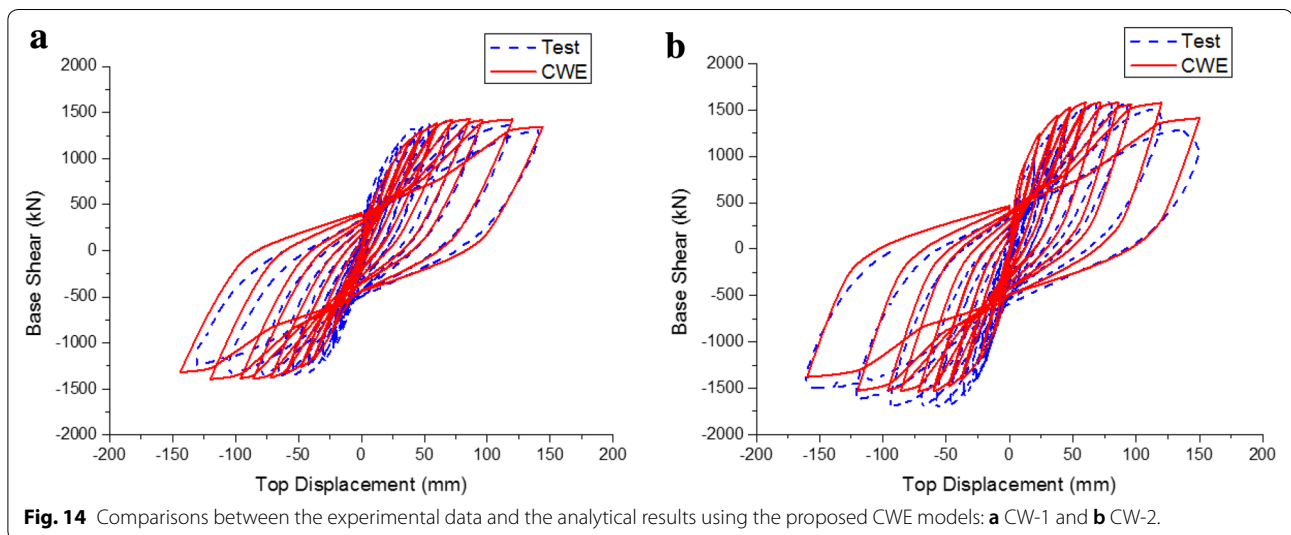
effectively demonstrate the reasonability of the CWE. The detailed design information of two coupled wall specimens regarding the mechanics properties of materials, physical dimensions, and reinforcement layout can be found in the literature (Lequesne 2011).
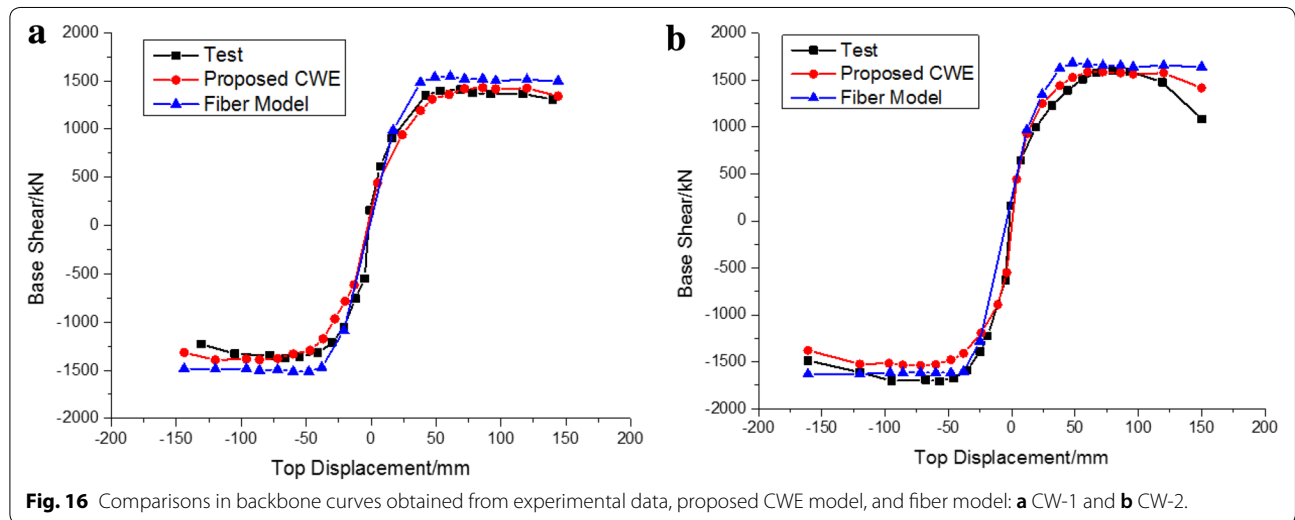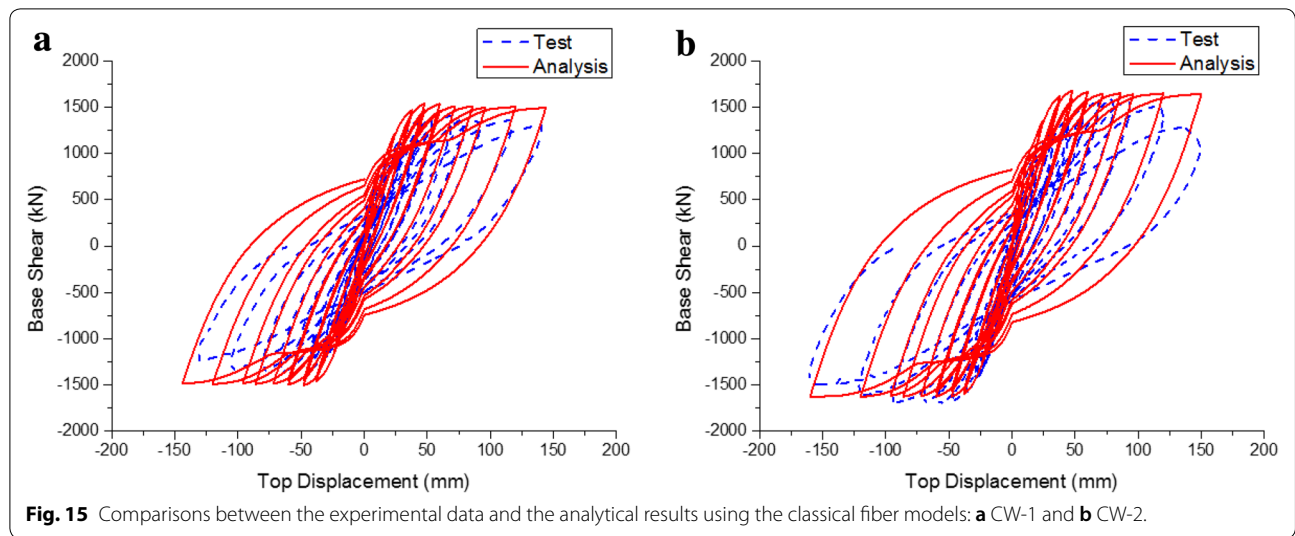
Comparisons between the hysteretic base shear force versus top displacement relation curves obtained from the experimental test and predicted by the proposed CWE are presented in Fig. 14. Figure 14 indicates that closer agreements in unload-reload paths, shapes of hysteretic loops, strength and stiffness deterioration, maximum shear forces, and backbone curves are reached using the proposed CWE. To illustrate the influence of

Fig. 13 Analytical model of RC coupled wall element (CWE).

nonlinear shear deformations of diagonally reinforced coupling beams and RC wall piers on the overall RC coupled wall systems, another modeling strategy that the sections of these two components both are simulated using the classical fiber models identical to the Sects. 3 and 4 is also utilized. The simulation results are compared with the experimental data in Fig. 15. Figure 15 demonstrates that the discrepancies in predicted and test backbone curves, hysteretic loops, and maximum shear forces are obvious. To illustrate the differences in

backbone curves, maximum shear forces, and energy dissipations predicted by the proposed CWE and fiber model, the associated analytical results are compared to corresponding experimental data respectively, which are presented in Figs. 16, 17, and 18. The backbone curve simulated using proposed CWE in Fig. 16a has a good agreement with the test one in predicted strength deterioration, yielding and maximum shear forces, while the fiber model overestimates the maximum shear force and cannot simulate the characteristic of strength deterioration. Figure 16b shows that the maximum shear force simulated from proposed CWE in the positive loading direction approximates to the test one but the result in the negative loading direction is underestimated, and that the fiber model overestimates the maximum shear force in the positive direction yet the result in the negative direction agrees with the test one well. This is because the test result for specimen CW-2 has an apparent discrepancy in the positive and negative loading directions, and the proposed and fiber models both are approximately symmetric in the positive and negative directions. The strength deterioration is captured well by the proposed CWE but fails to be simulated using the fiber model. The maximum shear force in each number of loading cycle is compared with the experimental data in Fig. 17. Figure 17a indicates that the proposed CWE is able to accurately predict the maximum shear force in each loading cycle and the fiber model overestimates the one, while Fig. 17b shows an apparent dispersion. The reason is identical to that described above. Hysteretic energy dissipation is an important indicator in reflecting nonlinear behavior of component. Thus the energy dissipation in each of loading cycle numbers is also compared in Fig. 18. Both Fig. 18a and b demonstrate that the

Fig. 14 Comparisons between the experimental data and the analytical results using the proposed CWE models: **a** CW-1 and **b** CW-2.

Fig. 15 Comparisons between the experimental data and the analytical results using the classical fiber models: **a** CW-1 and **b** CW-2.

Fig. 16 Comparisons in backbone curves obtained from experimental data, proposed CWE model, and fiber model: **a** CW-1 and **b** CW-2.

proposed CWE model can capture the energy dissipation well in each number of cyclic loading and the fiber model overestimates the result.

This reversed cyclic loading test sets up two actuators located at 2- and 4-story of coupled wall specimens respectively, the two actuators can record the observed shear forces (Lequesne 2011). To discuss the advantage of the proposed CWE in detail, the quantifications of maximum shear forces at lower actuator, upper actuator, and base, as well as overall energy dissipation from proposed CWE and classic fiber models are also considered as indicators and compared with corresponding experimental data respectively, which are summarized in Table 5.

The curvature and shear distortion of six monitored sections (six Gauss–Lobatto integration points) in the

first story of specimen CW-1 are presented in Figs. 19 and 20 respectively. Figure 19 shows that curvatures are large enough to cause flexural yielding throughout the first story. There is a clear trend of large curvature ductility near the foundation, and diminishing ductility demands further up the wall. Comparing the curvatures calculated for the compression wall to those of the tension wall, larger curvatures were observed in the compression wall than in the tension wall throughout the first story. The primary explanation for the larger curvatures recorded in the compression walls is that the separate wall foundations allow for coupling beams to rotate towards the compression wall. This rotation reduces the deformation demands placed on the tension wall and requires the plastic hinge region in the compression wall
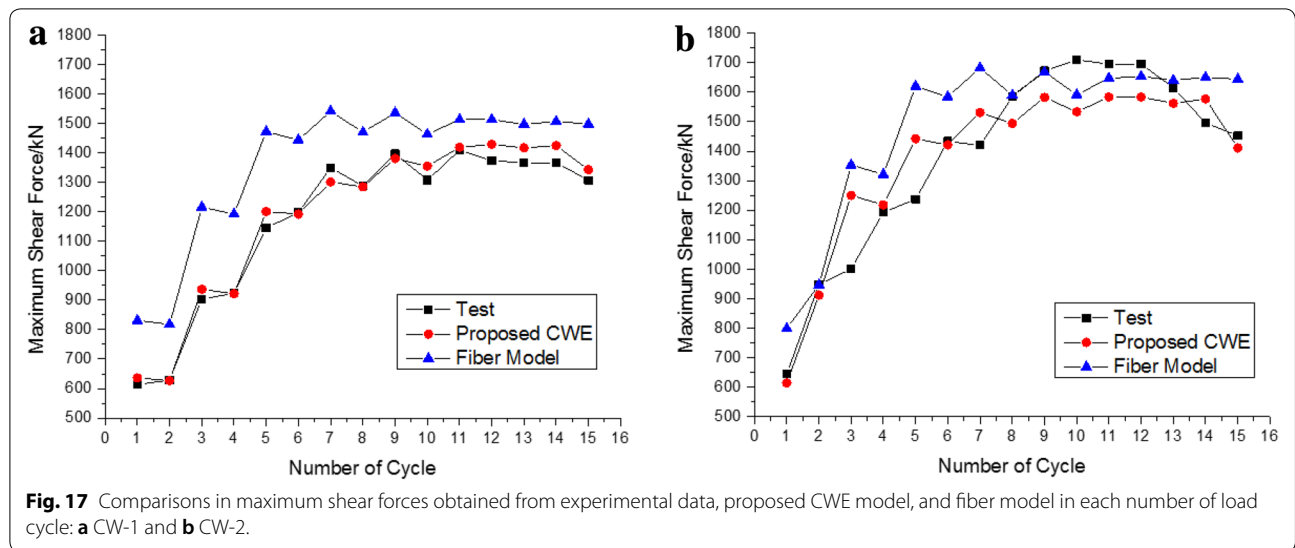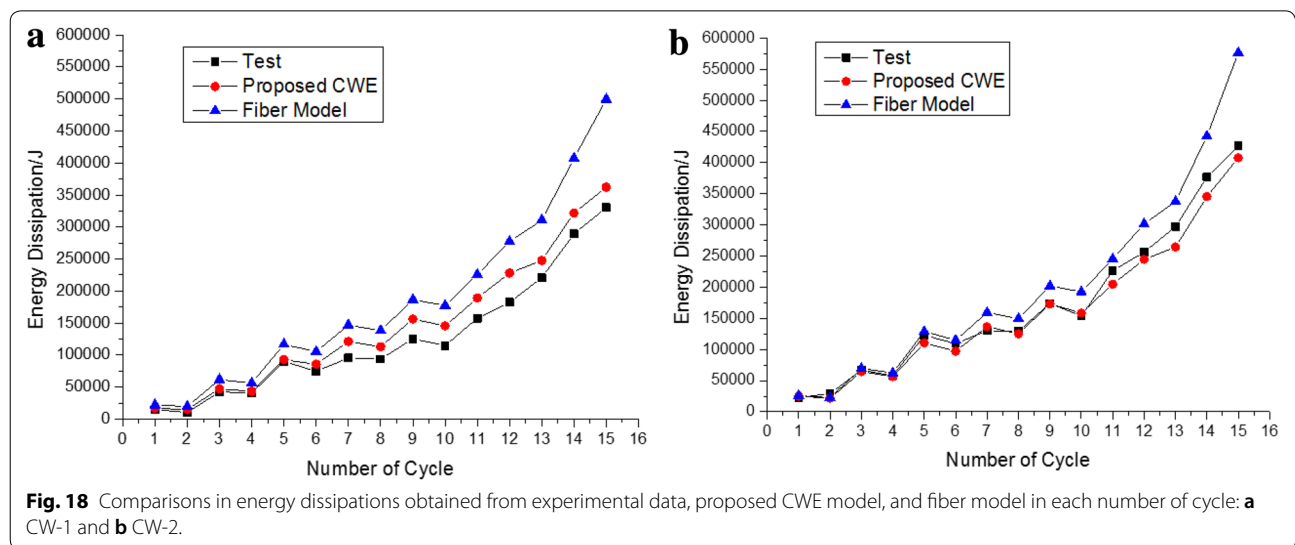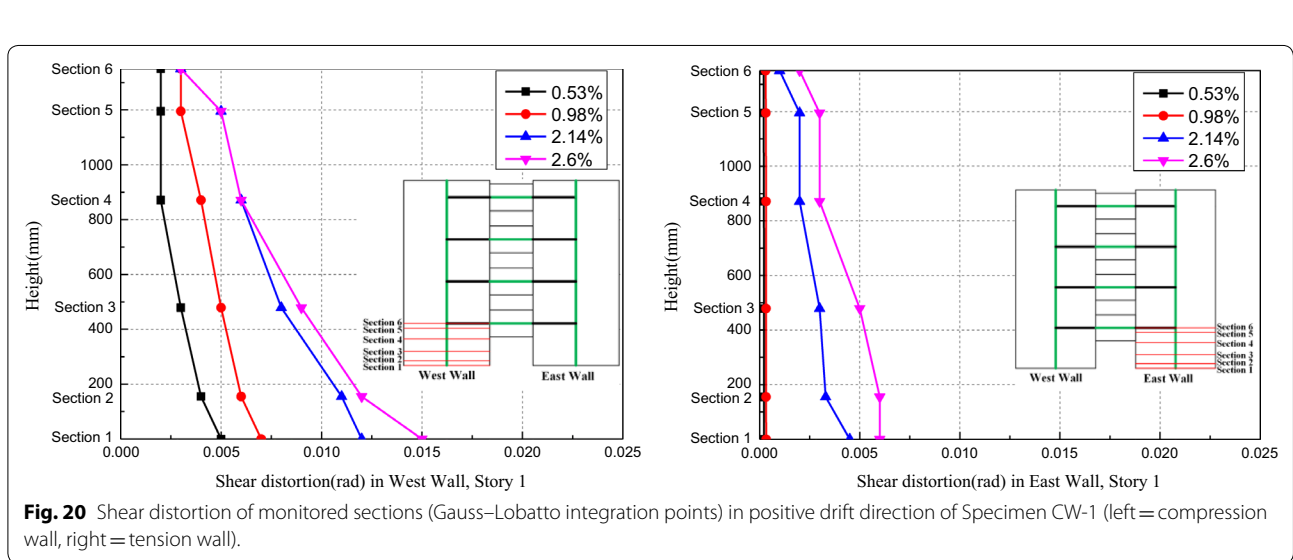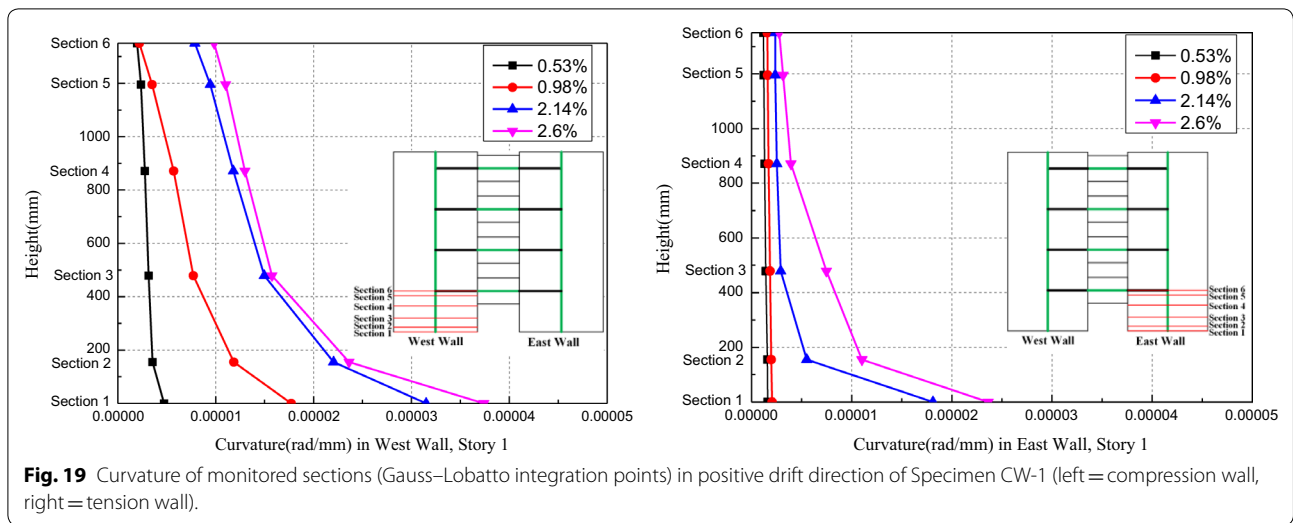
Fig. 17 Comparisons in maximum shear forces obtained from experimental data, proposed CWE model, and fiber model in each number of load cycle: **a** CW-1 and **b** CW-2.

Table 5 The comparisons of selected indicators from CWE and test ones.

Specimen	Type	Lower actuator maximum shear/kN		Upper actuator maximum shear/kN		Base maximum shear/kN		Energy dissipation/J
		Positive	Negative	Positive	Negative	Positive	Negative	
CW-1	Test	423	− 423	987	− 973	1410	− 1396	443,108
	CWE	436	− 436	992	− 977	1428	− 1413	475,195
	Fiber Model	458	− 449	1063	− 1051	1521	− 1500	558,292
CW-2	Test	596	− 646	1014	− 1064	1610	− 1710	562,755
	CWE	579	− 579	1003	− 987	1582	− 1566	595,810
	Fiber Model	637	− 612	1051	− 1031	1688	− 1643	676,166

Fig. 18 Comparisons in energy dissipations obtained from experimental data, proposed CWE model, and fiber model in each number of cycle: **a** CW-1 and **b** CW-2.

to develop larger deformations than in the tension wall. The shear distortion in the first story of specimen CW-1 is shown in Fig. 20. It indicates that the shear distortion generally increased closer to the foundation. The larger shear distortion near the foundation was primarily due to a reduction in the wall shear stiffness caused by larger

Fig. 19 Curvature of monitored sections (Gauss–Lobatto integration points) in positive drift direction of Specimen CW-1 (left = compression wall, right = tension wall).

Fig. 20 Shear distortion of monitored sections (Gauss–Lobatto integration points) in positive drift direction of Specimen CW-1 (left = compression wall, right = tension wall).

flexural rotations near the base of the wall. A general trend of larger shear distortion in the compression wall was observed. The primary cause is the shift of shear force to the compression wall, which has been well documented in coupled wall systems test (Santhakumar 1974; Shiu et al. 1981; Ozselcuk 1989; Lequesne 2011; Lehman et al. 2013).

Figure 21 indicates that the simulated maximum shear forces of CW-1 from proposed model whether in the positive direction or negative direction have higher level of agreement than those obtained by classic fiber model. However, as the corresponding relationships between forces and deformations for CW-2 from test are asymmetric, the results simulated by the proposed CWE are just approximation to the test ones in the positive

direction, while those in the negative are not perfect fit, as shown in Fig. 22.

From the viewpoint of hysteretic energy dissipation, the advantage of the proposed CWE is much more apparent, while the energy absorption capacity simulated by classical fiber model shows a significant error. This phenomenon is mainly caused by the situation where the proposed CWE accounts for nonlinear shear effect at both coupling beams and shear walls levels and thus the simulated results include the extra part induced by shear response of coupled walls; the classic fiber model however is just able to model the interaction between axial and flexural response, and the shear response fails to be represented by this scheme. Therefore, the nonlinear response received from the former is more close to the actual test
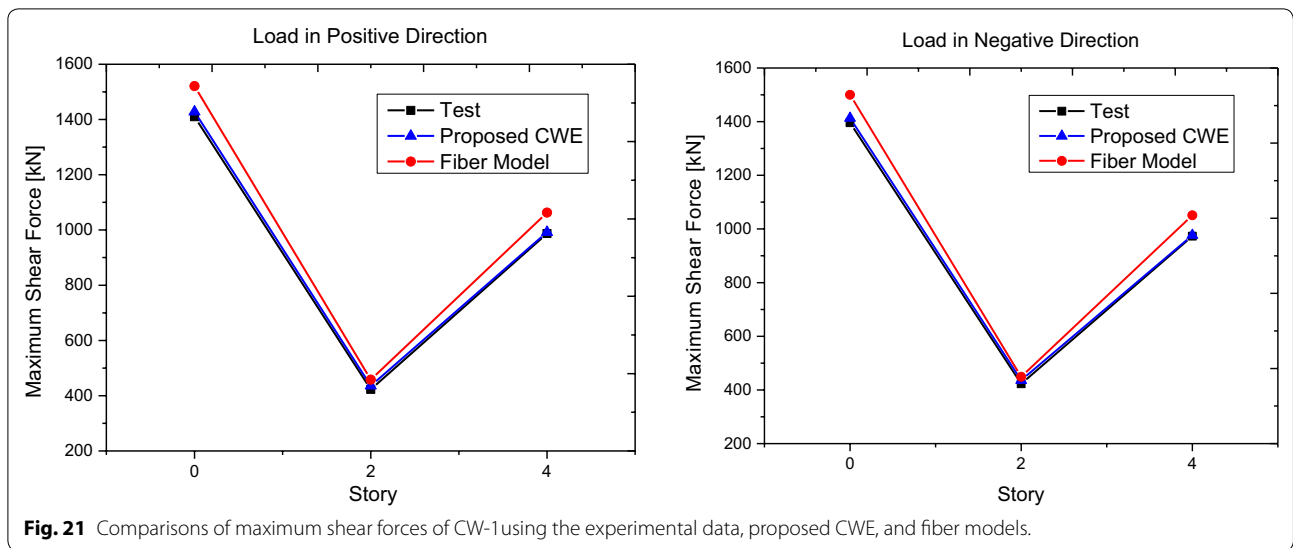
Fig. 21 Comparisons of maximum shear forces of CW-1using the experimental data, proposed CWE, and fiber models.
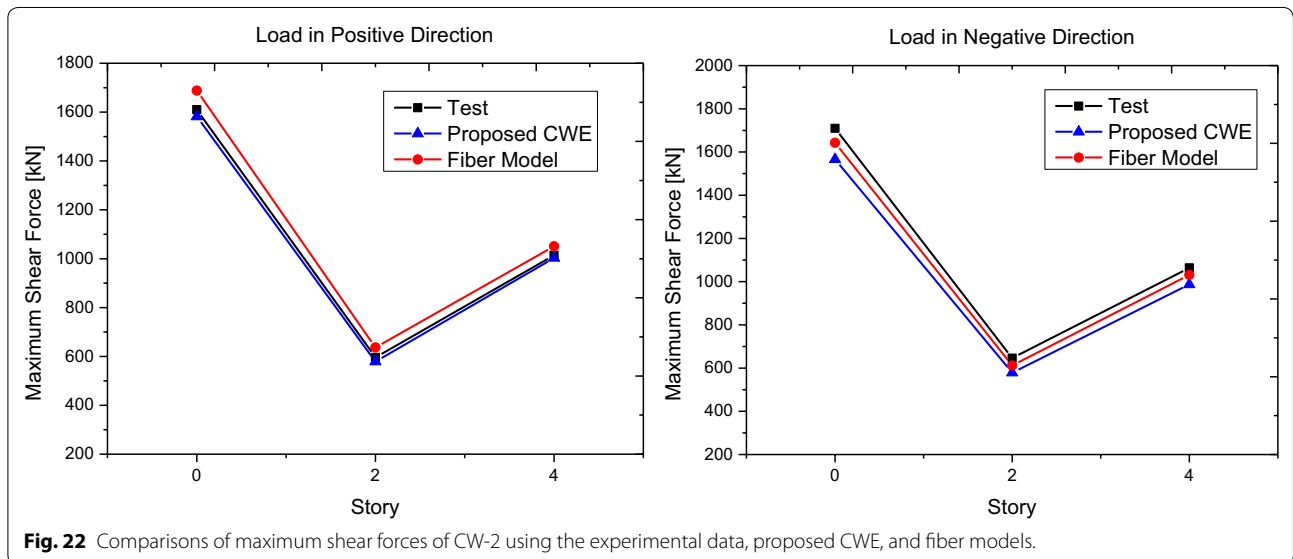

Fig. 22 Comparisons of maximum shear forces of CW-2 using the experimental data, proposed CWE, and fiber models.

response than that from the latter. To clearly recognize the difference between the proposed methodology and classic fiber method, the detailed error quantifications of the selected indicators are also presented in the Table 6.

6 Discussion of the Models

The modified force-based fiber element (MFBFE) takes into account the element shear deformation, which enables this element to handle a coupled axial–shear–bending response at the element level. At the section level, a novel shear model for RC coupling beams (MFBBE) and an existed shear model for RC shear walls (MFBWE) are respectively added to MFBFE to simulate nonlinear responses of these two key components. The analytical

model for RC coupled walls (CWE) is developed through integrating the proposed models of these two key components. The proposed models are validated against coupling beams, shear walls and coupled walls specimens under cyclic loading, compared to the very limited experimental data. It is found that the models can provide a more precise prediction on the response compared with the traditional fiber element, in regards to the initial stiffness, peak shear strength, strength and stiffness degradation, and especially pinching effects.

However, the proposed models have several limitations. First, curvature and shear distortion are uncoupled at the section level and sectional analysis under flexure assumes plane-sections-remain plane in these models.

Table 6 The error comparisons of the selected indicators.

Specimen	Type	Errors in lower actuator maximum shear		Errors in upper actuator maximum shear		Errors in base maximum shear		Errors in energy dissipation
		Positive	Negative	Positive	Negative	Positive	Negative	
CW-1	Test	0	0	0	0	0	0	0
	CWE	3.07%	3.07%	0.51%	0.41%	1.28%	1.22%	7.24%
	Fiber model	8.27%	6.15%	7.70%	8.02%	7.87%	7.45%	25.99%
CW-2	Test	0	0	0	0	0	0	0
	CWE	− 2.85%	− 10.37%	− 1.08%	− 7.23%	− 1.74%	− 8.42%	5.87%
	Fiber model	6.88%	− 5.26%	2.64%	− 3.10%	4.20%	− 3.92%	20.15%

This approach, although practical and sufficient for many cases, will not represent the actual mechanical behavior of coupling beams with diagonal cracking and "real" shear failure (diagonal tension or compression), and cannot be considered as generalized approach to represent the physical behavior of coupling beams. Wall piers in coupled walls will undergo significant fluctuations in axial loads during seismic responses, and uncoupling their nonlinear shear behavior from their axial/flexural response at the section level is also not a generalized approach for characterization of their shear behavior. Second, the Menegotto–Pinto reinforcement model is employed for the cyclic behavior. Although the model can effectively reproduce the Bauschinger effect, bar buckling, and bar fracture because of high tensile strain, it fails to account for fracture because of fatigue. Furthermore, modeling approaches have not been sufficiently validated against local deformation characteristics (rotations, curvatures, strains) because of a lack of detailed experimental data. In addition, the proposed models are validated only under cyclic loading in this study, the validation of nonlinear dynamic analysis should be further studied.

7 Conclusions

A novel analytical model for nonlinear simulation of RC coupled wall systems under reversed cyclic loading is proposed in this paper. The model incorporates two key components, which are analytical models of RC shear wall and diagonally reinforced coupling beams. The critical issues associated with the numerical modeling schemes for these two key components are discussed in detail and depth through comparisons using the observed experimental data and analytical results. To validate accuracy and accuracy of the proposed analytical model for diagonally reinforced coupling beams, four experimental specimens are used as analytical examples, one of which is analyzed by different modeling strategies to find out the optimum modeling method including definition of four control points in the backbone curve, utilization of Mander and Legeron confined concrete models, and effect of sectional shear deformation, and other specimens are thus simulated by the selected optimum modeling scheme. Good agreements are achieved for all of these four specimens through comparisons of hysteretic curves analyzed from analytical means and observed by experimental tests. This outcome confirms that the proposed analytical model is able to capture the nonlinear behavior observed in the tests including strength and stiffness deterioration, maximum shear force, and pinching characteristic.

For the nonlinear simulation of RC shear wall, the modeling method similar to the diagonally reinforced coupling beams is adopted to simulate two 1/2 scale RC shear wall specimens. Validation of accuracy and efficiency via comparisons between the experimental data and the simulated results is received. This illustrates the reasonability of the proposed RC shear wall model in modeling nonlinear response of RC shear wall, and further demonstrates that the validated modeling method is appropriate to the simulation of RC shear wall.

Using the validated modeling strategy, an overall RC coupled wall system model, integrating the proposed analytical models of diagonally reinforced coupling beams and RC shear wall is presented to simulate two large-scaled RC coupled wall specimens. The predicted results including degradation of stiffness and strength, moderate pinching behavior, hysteretic energy dissipation as well as maximum shear force compared to corresponding test findings show a good level of agreement, verifying that the proposed RC coupled wall model is capable of describing the nonlinear behavior observed from test.

In order for indicating that the influence of nonlinear shear deformations from diagonally reinforced coupling beams and RC wall piers on the nonlinear response of overall RC coupled wall systems is apparent, another modeling scheme in terms of classical fiber model is

Du *et al. Int J Concr Struct Mater*   (2019) 13:34

Page 25 of 26

adopted to simulate these two RC coupled walls. Note that all of the material models as well as various parameters are identical other than the adoption of the shear models for diagonally reinforced coupling beams and RC shear wall. Comparisons between experimental data and simulation results show that the predicted nonlinear behavior characteristics including hysteresis energy dissipation, maximum shear force, and strength and stiffness deterioration have obvious discrepancy with the corresponding experimental findings. This further proves that the nonlinear shear deformations of coupling beams and wall piers in a coupled wall system are not able to be ignored.

Authors' contributions
KD, HL, and JB contributed to methodology, software, formal analysis and writing original draft. JS contributed to the supervision and discussion. All authors read and approved the final manuscript.

Author details
[1] Key Laboratory of Earthquake Engineering and Engineering Vibration, Institute of Engineering Mechanics, China Earthquake Administration, Harbin 150080, China. [2] Key Laboratory of New Technology for Construction of Cities in Mountain Area, Chongqing University, Ministry of Education, Chongqing 400045, China.

Competing interests
The authors declare that they have no competing interests.

Availability of data and materials
Please contact author for data requests.

Publisher's Note
Springer Nature remains neutral with regard to jurisdictional claims in published maps and institutional affiliations.

References
ACI 318-11. (2011). Building code requirements for structural concrete and commentary. ACI Committee 318, Farmington Hills.

Almeida, J. P., Correia, A. A., & Pinho, R. (2015). Force-based higher-order beam element with flexural–shear–torsional interaction in 3D frames. Part II: Applications. *Engineering Structures, 89,* 218–235.

Bitar, I., Grange, S., Kotronis, P., & Benkemoun, N. (2018). A comparison of displacement-based Timoshenko multi-fiber beams finite element formulations and elasto-plastic applications. *European Journal of Environmental and Civil Engineering, 22*(4), 464–490.

Correia, A. A., Almeida, J. P., & Pinho, R. (2015). Force-based higher-order beam element with flexural–shear–torsional interaction in 3D frames. Part I: Theory. *Engineering Structures, 89,* 204–217.

Dazio, A., Beyer, K., & Bachmann, H. (2009). Quasi-static cyclic tests and plastic hinge analysis of RC structural walls. *Engineering Structures, 31*(7), 1556–1571.

Eljadei, A. A., & Harries, K. A. (2014). Design of coupled wall structures as evolving structural systems. *Engineering Structures, 73*(73), 100–113.

Feng, D. C., & Xu, J. (2018). An efficient fiber beam-column element considering flexure-shear interaction and anchorage bond-slip effect for cyclic analysis of RC structures. *Bulletin of Earthquake Engineering, 16*(11), 5425–5452.

Ferreira, D., Bairán, J. M., Mari, A. R., & Faria, R. (2014). Nonlinear analysis of RC beams using a hybrid shear–flexural fibre beam model. *Engineering Computations, 31*(7), 1444–1483.

Fisher, A. W., Collins, M. P., & Bentz, E. C. (2018). *Influence of shear on deformations of coupling beams* (pp. 1156–1163). High Tech Concrete: Where Technology and Engineering Meet.

Fox, M. J., Sullivan, T. J., & Beyer, K. (2014). Capacity design of coupled RC walls. *Journal of Earthquake Engineering, 18*(5), 735–758.

Galano, L., & Vignoli, A. (2000). Seismic behavior of short coupling beams with different reinforcement layouts. *ACI Structural Journal, 97*(6), 876–885.

Gerin, M., Adebar, P. (2004). Accounting for shear in seismic analysis of concrete structures. In: Proc., 13th World Conf. on Earthquake Engineering.

Gong, B., & Fang, E. (1988a). Behavior of reinforced concrete coupling beams between shear walls under cyclic loading. *Journal of Building Structure, 9*(1), 34–40. **(in Chinese)**.

Gong, B., & Fang, E. (1988b). Experimental investigation and full-range analysis of reinforced concrete coupling beams between shear walls. *Building Science, 4*(4), 41–45. **(in Chinese)**.

Gulec, C. K., Whittaker, A. S. (2009). Performance-based assessment and design of squat reinforced concrete shear walls. Technical Report MCEER-09-0010.

Han, S. W., Lee, C. S., Shin, M., et al. (2015). Cyclic performance of precast coupling beams with bundled diagonal reinforcement. *Engineering Structures, 93,* 142–151.

Harries, K. A., Moulton, J. D., & Clemson, R. L. (2004). Parametric study of coupled wall behavior—implications for the design of coupling Beams. *Journal of Structural Engineering, 130*(3), 480–488.

Hindi, R. A., & Hassan, M. A. (2004). Shear capacity of diagonally reinforced coupling beams. *Engineering Structures, 26*(10), 1437–1446.

Hines E. M., Dazio A., & Seible F. (2002). Seismic performance of hollow rectangular reinforced concrete piers with highly-confined boundary elements phase III: Web crushing tests. *Rep. No. SSRP-2001/27*; Univ. of California, San Diego, p 239.

Hines E. M., Seible F., & Priestley, M. J. N. (1995). Cyclic tests of structural walls with highly-confined boundary elements. *Rep. No. SSRP-99/15*; Univ. of California, San Diego, p 266.

Hirosawa, M. (1975). Past experimental results on reinforced concrete shear walls and analysis on them. Kenchiku Kenkyu Shiryo, No. 6, Building Research Institute, Ministry of Construction **(in Japanese)**.

Hung, C. C. (2012). Modified full operator hybrid simulation algorithm and its application to the seismic response simulation of a composite coupled wall system. *Journal of Earthquake Engineering, 16*(6), 2575.

Hung, C. C., & El-Tawil, S. (2011). Seismic behavior of a coupled wall system with HPFRC materials in critical regions. *Journal of Structural Engineering, 137*(12), 1499–1507.

Ibarra, L. F., Medina, R. A., & Krawinkler, H. (2005). Hysteretic models that incorporate strength and stiffness deterioration. *Earthquake Engineering and Structural Dynamics, 34*(12), 1489–1511.

Jun, Z., Kou, L., Fuqiang, S., Xiangcheng, Z., & Chenzhe, S. (2018). An analytical approach to predict shear capacity of steel fiber reinforced concrete coupling beams with small span–depth ratio. *Engineering Structures, 171,* 348–361.

Kabeyasawa, T., Shiohara, T., Otani, S., et al. (1982). Analysis of the full-scale seven story reinforced concrete test structure: Test PSD3. In: Proc. 3rd JTCC, US-Japan Cooperative Earthquake Research Program.

Kim, D. K. (2016). Seismic response analysis of reinforced concrete wall structure using macro model. *International Journal of Concrete Structures & Materials, 10*(1), 99–112.

Kim, J., & Choi, Y. (2017). Seismic capacity design and retrofit of reinforced concrete staggered wall structures. *International Journal of Concrete Structures and Materials, 11*(2), 285–300.

Kolozvari, K., Orakcal, K., & Wallace, J. W. (2015). Modeling of cyclic shear–flexure interaction in reinforced concrete structural walls. I: Theory. *Journal of Structural Engineering, 141*(5), 04014135.

Legeron, F., & Paultre, P. (2003). Uniaxial confinement model for normal- and high-strength concrete columns. *Journal of Structural Engineering, 129*(2), 241–252.

Lehman, D. E., Turgeon, J. A., Birely, A. C., et al. (2013). Seismic behavior of a modern concrete coupled wall. *Journal of Structural Engineering, 139*(8), 1371–1381.

Lequesne, R.D. (2011). Behavior and design of high-performance fiber-reinforced concrete coupling beams and coupled-wall systems. *Ph.D Dissertation,* Michigan: The University of Michigan.

Lequesne, R. D., Parra-Montesinos, G. J., & Wight, J. K. (2012). Seismic behavior and detailing of high-performance fiber-reinforced concrete coupling beams and coupled wall systems. *Journal of Structural Engineering, 139*(8), 1362–1370.

Lowes, N. L., Lehman, E. D., Birely, C. A., Kuchma, A. D., Marley, P. K., & Hart, R. C. (2012). Earthquake response of slender planar concrete walls with modern detailing. *Engineering Structures, 43,* 31–47.

Lucchini, A., Franchin, P., & Kunnath, S. (2017). Failure simulation of shear-critical RC columns with non-ductile detailing under lateral load. *Earthquake Engineering and Structural Dynamics, 46*(5), 855–874.

Mander, J. B., Priestley, M., & Park, R. (1988). Theoretical stress-strain model for confined concrete. *Journal of Structural Engineering, 114*(8), 1804–1826.

Marini, A., & Spacone, E. (2006). Analysis of reinforced concrete elements including shear effects. *ACI Structural Journal, 103*(5), 645–655.

Massone, L. M., Orakcal, K., & Wallace, J. W. (2004). Load-deformation responses of slender reinforced concrete walls. *ACI Structural Journal, 101*(1), 103–113.

Massone, L. M., Orakcal, K., & Wallace, J. W. (2009). Modeling of squat structural walls controlled by shear. *ACI Structural Journal, 106*(5), 646–655.

MATLAB User's Guide (2014). The MathWorks Inc.

Menegotto, M., & Pinto, P. E. (1973). *Method of analysis for cyclically loaded RC plane frames including changes in geometry and non-elastic behavior of elements under combined normal force and bending*. Lisbon: International Association for Bridge and Structural Engineering.

Ozselcuk A. R. (1989). Experimental and analytical studies of coupled wall structures. Ph.D. dissertation, Univ. of California, Berkeley, CA.

Paulay, T. (1971). Coupling beams of reinforced concrete shear walls. *Journal of Structural Engineering, ASCE, 97*(3), 843–862.

Paulay, T., Binney J. R. (1974). Diagonally reinforced coupling beams of shear walls. *Shear in Reinforced Concrete, SP-42*. Farmington Hills, MI: American Concrete Institute, p. 579–98.

Petrangeli, M., Pinto, P. E., & Ciampi, V. (1999). Fiber element for cyclic bending and shear of RC structures. I: Theory. *Journal of Engineering Mechanics, 125*(9), 994–1001.

Saatcioglu, M., Derecho, A. T., & Corley, W. G. (1983). Modelling hysteretic behaviour of coupled walls for dynamic analysis. *Earthquake Engineering and Structural Dynamics, 11*(5), 711–726.

Said, A., Elmorsi, M., & Nehdi, M. (2005). Non-linear model for reinforced concrete under cyclic loading. *Magazine of Concrete Research, 57*(4), 211–224.

Santhakumar, A. R. (1974). The ductility of coupled shear walls. Ph.D. dissertation, Univ. of Canterbury, Christchurch, New Zealand.

Sayre, B. (2003). Performance evaluation of steel reinforced shear walls. M.S. thesis, Univ. of California, Los Angeles.

Scott, B., Park, R., & Priestley, M. (1982). Stress-strain behavior of concrete confined by overlapping hoops at low and high strain rates. *ACI Journal Proceedings, 79*(1), 13–27.

Shiu, K. N., Aristizabal-Ochoa, J. D., Barney, G. B., Fiorato, A. E., & Corley W. G. (1981). Earthquake resistant structural walls: Coupled wall tests. *Rep. to National Science Foundation*; Construction Technology Laboratories, Portland Cement Association, Stokie, IL.

Spacone, E., Filippou, F. C., & Taucer, F. F. (1996). Fiber beam-column model for non-linear analysis of RC frames: part i. formulation. *Earthquake Engineering and Structural Dynamics, 25*(7), 711–726.

Takayanagi, T., & Schnobrich, W. C. (1979). Non-linear analysis of coupled wall systems. *Earthquake Engineering and Structural Dynamics, 7*(1), 1–22.

Tassios, T. P., Moretti, M., & Bezas, A. (1996). On the behavior and ductility of reinforced concrete coupling beams of shear walls. *ACI Structural Journal, 93*(6), 711–720.

Thomsen, J. H., & Wallace, J. W. (2004). Displacement-based design procedures for slender reinforced concrete structural walls—Experimental verification. *Journal of Structural Engineering, 130*(4), 618–630.

Vallenas J. M., Bertero V. V., & Popov E. P. (1979). Hysteretic behaviour of reinforced concrete structural walls. *Rep. No. UBC/EERC-79/20*; Univ. of California, Berkeley, CA, 234.

Vulcano, A., Bertero, V. V., Colotti, V. (1988). Analytical modeling of RC structural walls. In: Proc., 9th World Conf. on Earthquake Engineering.

Vuran, E., & Aydınoğlu, M. N. (2016). Capacity and ductility demand estimation procedures for preliminary design of coupled core wall systems of tall buildings. *Bulletin of Earthquake Engineering, 14*(3), 721–745.

Wallace, J. W. (2007). Modeling issues for tall reinforced concrete core wall buildings. *Structural Design of Tall and Special Buildings, 16*(5), 615–632.

Wang T. Y., Bertero V. V., & Popov E. P. (1975). Hysteretic behaviour of reinforced concrete framed walls. *Rep. No. UBC/EERC-75/23*; Univ. of California, Berkeley, CA, 367.

Zhang, H., Lv, X., Lu, L., et al. (2007). Influence of boundary element on seismic behavior of reinforced concrete shear walls. *Earthquake Engineering and Engineering Vibration, 27*(01), 92–98. **(in Chinese)**.

Zimos, D. K., Mergos, P. E., & Kappos, A. J. (2018). Modelling of R/C members accounting for shear failure localisation: Finite element model and verification. *Earthquake Engineering and Structural Dynamics, 47*(7), 1631–1650.